Studies of Beamline Instrumentation in the NOνA Test Beam Experiment

A thesis submitted in partial fulfillment of
the requirement for the degree of
Bachelor of Science in Physics
from the College of William and Mary in Virginia,

by

Finnian R. Mayhew

Patricia L. Vahle

Advisor: Prof. Patricia L. Vahle

Todd Averett

Prof. Todd D. Averett

Williamsburg, Virginia
May 2020

Contents

Acknowledgments

Thank you to all the physics professors I've been lucky enough to take classes with during my time at William & Mary: Drs. Tracy, Sher, Vahle, Novikova, Kordosky, Armstrong, Orginos, Cooke, Averett, Monahan, and Vahala. Thank you especially to Dr. Vahle for your long-running guidance and support of my research. Thank you to the scientists at the NOνA collaboration who've helped me tremendously, especially Mike Wallbank, Erika Catano-Mur, and Teresa Lackey.

List of Figures

List of Tables

Abstract

This work catalogs two related studies of the NOνA Test Beam beamline, one of which was conducted before the redeployment of the experiment's time of flight detectors on December 10, 2020 and the other of which was conducted after the redeployment.

First, pre-redeployment, this work characterizes and attempts to diagnose a discrepancy between the expected and observed time of flight of particles through the beamline. Particle momentum and time of flight are reconstructed for a preexisting dataset of particle events, then each event is identified with a particle species by a combination of the event's location in a phase space consisting of reconstructed time of flight, reconstructed momentum, and the associated trigger state of the experiment's Cherenkov counter. Expectation curves in phase space for each species are drawn as prescribed by the relativistic momentum equation. The expectation curves and the data are compared to characterize the time of flight discrepancy, and transformations to the expectation curves following from associated hypotheses of the cause of the discrepancy are compared in an attempt to diagnose the discrepancy. This study concludes when the discrepancy is found to be absent after the redeployment.

Second, post-redeployment, this work uses the same techniques to characterize and calibrate out a discrepancy between the expected and observed time of flight of particles through the beamline measured using the experiment's Silicon Photomultiplier detector as the downstream detector, in preparation for the introduction of an additional arm as a source of time of flight data for use in particle identification.

Chapter 1

Context

1.1 Neutrino Oscillation

Quantum mechanics, through the mathematical mechanism of linear algebra, tells us that any particular subatomic particle can at any time be described as some "mixture" of basis states. For neutrinos, there are two bases: the "flavor basis" and the "mass basis." The elements of the flavor basis — the "flavor states" ν_e, ν_μ, and ν_τ — are the eigenvectors of the weak interaction, which pairs each neutrino with its subscripted lepton, and the elements of the mass basis — the "mass states" ν_1, ν_2, and ν_3 — are the eigenvectors of the free particle Hamiltonian with respective masses m_1, m_2, and m_3. Every flavor state is a linear combination of the mass states, and every mass state is a linear combination of the flavor states.

The mixing is described mathematically by the PMNS matrix U such that

$$\begin{pmatrix} \nu_e \\ \nu_\mu \\ \nu_\tau \end{pmatrix} = U \begin{pmatrix} \nu_1 \\ \nu_2 \\ \nu_3 \end{pmatrix} = \begin{pmatrix} U_{e1} & U_{e2} & U_{e3} \\ U_{\mu 1} & U_{\mu 2} & U_{\mu 3} \\ U_{\tau 1} & U_{\tau 2} & U_{\tau 3} \end{pmatrix} \begin{pmatrix} \nu_1 \\ \nu_2 \\ \nu_3 \end{pmatrix} \tag{1.1}$$

Neutrinos are detected in flavor states, which means that when a neutrino is measured it is entirely one of the flavor states. Because the mass states travel with different energies, which flavor state a neutrino is detected in depends periodically on its distance (or time) traveled. This periodic time dependence is neutrino oscillation. [1]

1.2 The NOνA Experiment

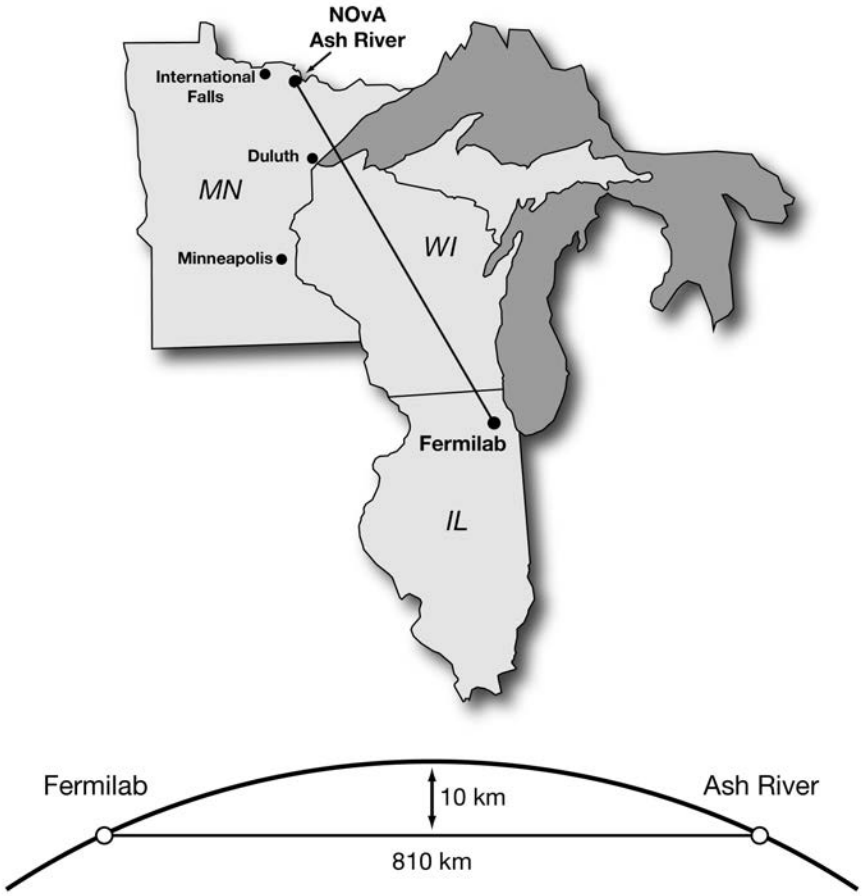

Figure 1.1: The NOνA beamline, starting at Fermilab in Chicago, IL and ending in Ash River, MN. Image: Fermilab Visual Media Services

NOνA stands for NuMI Off-axis ν_e Appearance (and NuMI stands for Neutrinos at the Main Injector). The experiment produces a neutrino beam using the Main Injector particle accelerator at Fermilab in Batavia, Illinois, measures it using a liquid scintillator detector called the Near Detector, and sends it through the Earth (see Fig. 1.1) to Ash River, Minnesota, where it is measured again using another liquid

scintillator detector called the Far Detector. The original NuMI beam consists of mostly ν_μ's, but by the time the beam reaches Minnesota a portion of those ν_μ's have oscillated into ν_e's. The experiment's two-detector and long-baseline design allows for the measurement of this proportion, which informs constraints on parameters in the PMNS matrix. [2]

1.3 The Test Beam Group

Generically, a test beam is a facility designed for the testing of detector components. Users request beams with specified properties, and by placing their machinery at the end of the beamline they study the machinery's response to different particles at known energies.

Figure 1.2: The Test Beam beamline, pre-redeployment (see Sec. 4). This is a fisheye view — the right and left of this image correspond to the front and back of a straight hallway. Image: Fermilab Creative Services

NOνA's Test Beam working group places a very small model of the Far Detector called the Test Beam Detector at the end of the beamline at the Fermilab Test Beam Facility, shown in Figs. 1.2 and 1.3. The group's goal is to model the Far Detector's response to the NuMI beam at the scale of individual particles by exposing the Test Beam Detector to the Test Beam beam, a tertiary beam from the Main Injector. The benefit of studying a model of the experiment's main detector instead of the

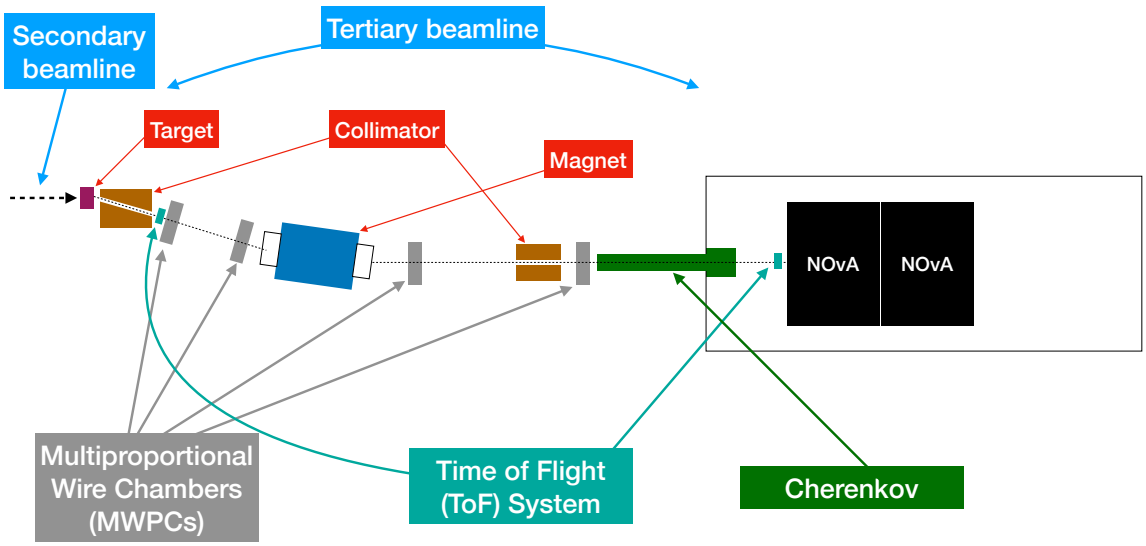

Figure 1.3: A diagram of the Test Beam beamline. Image: Mike Wallbank

main detector itself is that the model detector and its beamline can be tweaked and experimented on without disrupting the main detector and its beamline. Also, practically, there is no existing beam of charged particles that points at the Far Detector. [3]

Chapter 2

Theory

2.1 Particle ID

A critical step in analyzing detector response is identifying each particle event[1] in the detector with a particle species (deuteron, proton, kaon, pion, muon, or electron). This is done by distinguishing particles by their times of flight. Consider the relativistic momentum equation

$$p = \gamma m v$$

where p is the magnitude of a particle's momentum, γ is the Lorentz factor, m is the particle's rest mass, and v is the particle's speed. We want to solve for time of flight.

Let's rewrite γ to make all dependence on v explicit:

$$\gamma = \frac{1}{\sqrt{1 - v^2/c^2}}$$

where c is the speed of light. Then

$$p = \frac{mv}{\sqrt{1 - v^2/c^2}}$$

Solving for v yields

$$\frac{1}{v} = \sqrt{\frac{m^2}{p^2} + \frac{1}{c^2}}$$

[1] By "particle event" or "event," I mean the data structure that the online software creates when the instrumentation is triggered, not the physical particle.

By definition,

$$v = \frac{d}{ToF}$$

where d is the pathlength of the particle's trajectory and ToF is the particle's time of flight. Substituting, we arrive at our equation:

$$ToF(p) = d\sqrt{\frac{m^2}{p^2} + \frac{1}{c^2}} \tag{2.1}$$

Note that Eq. 2.1 is simply a rephrasing of the standard relativistic momentum equation — no other physics has been invoked. However, it makes clear that a particle's time of flight is dependent on the particle's mass and momentum.[2] The rest mass for each species is known, so for any given momentum we can predict a different time of flight for each species. Then if we can measure each particle's momentum and time of flight, we can compare the measured time of flight with the set of predicted times of flight for each species at the measured momentum and thereby identify the species of our particle. This is graphically equivalent to plotting an expectation curve for each species in a phase space consisting of time of flight and momentum and then noting which curve our particle falls nearest to when its event's data is placed in that phase space.

2.2 Momentum Reconstruction

Particle momentum is reconstructed (calculated from direct observations) using two pairs of wire chambers (that is, four total) along the beamline and a magnet placed between the pairs. Each wire chamber consists of a pair of orthogonal planes of

[2]Though it may seem an obvious choice to treat the pathlength d as constant (reasoning that all particles travel down the same beamline), it turns out this is not true! While each particle's trajectory is nearly identical in the parts of its journey for which it's traveling in a straight line (ignoring very small differences in pathlength due differently angled trajectories), the particles turn inside the beamline's magnet, and each particle's curving trajectory depends on both its species and its momentum. This is a small enough effect to note and ignore. [4]

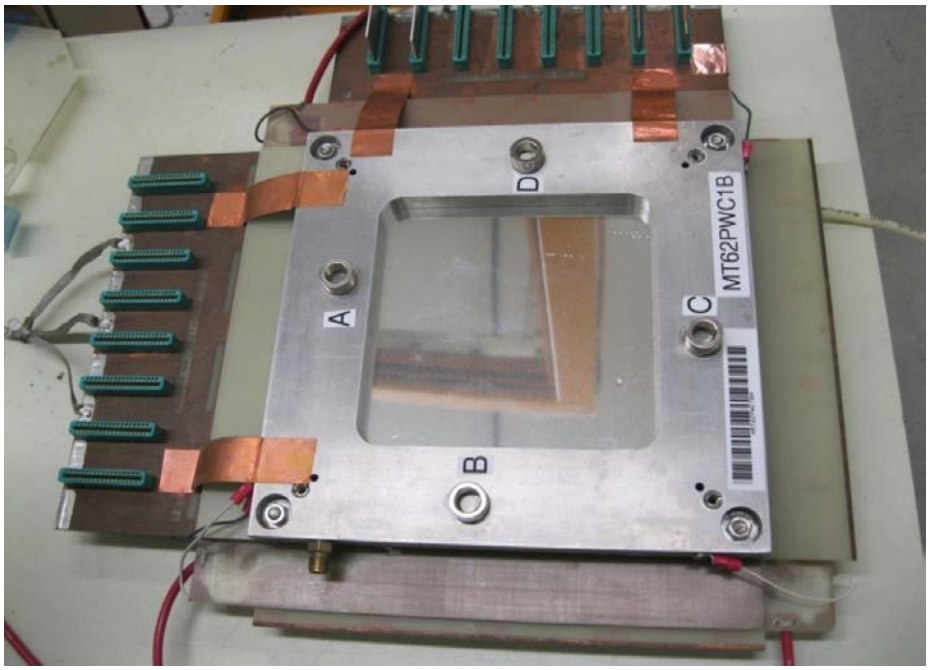

Figure 2.1: A wire chamber, used for momentum reconstruction as described in Sec. 2.2. Image: Fermilab Creative Services

parallel wires, shown in Fig. 2.1. The wires are submerged in a gas that ionizes when a charged particle passes through it and causes charge to collect on nearby wires. The closer to the particle's trajectory a wire falls the more charge it collects, so identifying the wire that collected the most charge in a plane gives one coordinate of the position of the particle's trajectory through the plane. Doing this for the orthogonal plane of wires within the same wire chamber gives the second coordinate of the position of the particle's trajectory through the plane, doing this for a pair of wire chambers gives the particle's full straight-line trajectory on one side of the magnet, and doing this for both pairs of wire chambers on either side of the magnet gives the change in the particle's trajectory due to the magnet. [5]

Next I'll describe in principal how the change in a particle's trajectory due to a magnetic field can reveal its momentum. The actual analytical technique the Test

Beam group uses for momentum reconstruction is more complex, but the details are not relevant for these particular studies.

From classical electromagnetism, we know that the force a magnetic field exerts on a moving charged particle is

$$\vec{F_B} = q\vec{v} \times \vec{B}$$

where q is the particle's charge, $\vec{v}$ is its velocity, and $\vec{B}$ is the magnetic field. If you can (ideally) orient a magnet in such a way that you set $\vec{B}$ always perpendicular to $\vec{v}$, the force equation simplifies to

$$F_B = qvB$$

and the magnet causes the particle's trajectory to trace a circular arc. Then the force from the magnet is centripetal:

$$F_c = \gamma m a_c = \frac{\gamma m v^2}{r}$$

$$F_B = F_c \implies qvB = \frac{\gamma m v^2}{r}$$

where r is the radius of curvature. Dividing by v,

$$qB = \frac{\gamma m v}{r}$$

And $p = \gamma m v$, so

$$p = rqB$$

Therefore if the particle's charge and the strength of the magnetic field are known, measuring the radius of curvature gives the particle's momentum. The change in a particle's trajectory due to the Test Beam magnet (reconstructed using the wire chambers) is similar to the radius of curvature, and the particle's momentum can be reconstructed using an equation similar to the equation above. [5]

2.3 Time of Flight Reconstruction

Particle time of flight is reconstructed using a pair of time of flight paddles, which are thin octagons of scintillator with a number of photomultiplier tubes (PMTs) at their corners placed along the beamline. When a particle passes through a paddle, the paddle's scintillator produces a small amount of light that is amplified and detected as current in the paddle's PMTs.

Mathematically, calculating the time of flight is simple:

$$ToF = t_{\mathrm{DS}} - t_{\mathrm{US}}$$

where t_{DS} is the time the particle is detected at the downstream paddle and t_{US} is the time the particle is detected at the upstream paddle. Complexity arises in determining the hit time for each paddle given the response of its PMTs and ensuring that the paddles' clocks are synchronized with each other. Currently, the process is to use constant fraction discrimination (described in Appendix A) to determine a hit time for each PMT and then average or take the earliest of the hit times from the PMTs within each paddle to determine the hit time for the paddle as a whole. In order to synchronize paddles' clocks, there are a number of electronic and physical delays that must be measured and accounted for, discussed in Sec. 5.1.2. [5]

2.4 Cherenkov Counting

Due to their relatively similar masses, in the momentum range of interest (~ 1 GeV/c) electrons are measured with very similar times of flight to pions and muons. As a consequence a particle cannot be identified as an electron solely by its location in momentum and time of flight phase space. An piece of data is needed to distinguish electrons from the other species.

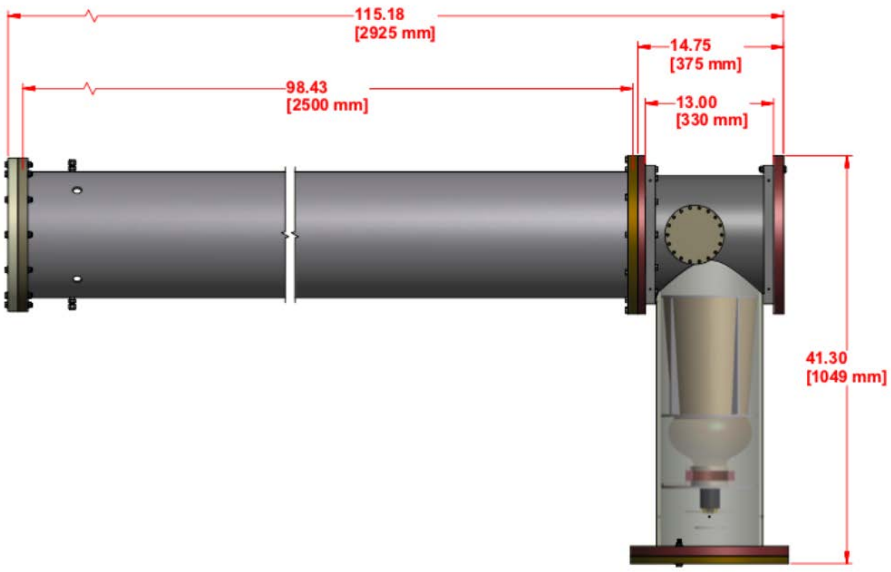

Figure 2.2: A Cherenkov counter, used identify electrons as described in Sec. 2.4. Image: The University of Texas at Austin

At the very end of the beamline is a Cherenkov counter, shown in Fig. 2.2. The counter is pressurized in such a way that in the relevant momentum range only electrons move faster than light in the medium. When a particle moves faster than light in a medium, it emits a characteristic light called Cherenkov radiation, analogous to a sonic boom. If the counter's PMT detects this light, it definitively identifies the relevant particle event with an electron. [6]

Chapter 3

First Study: Pre-redeployment ToF Discrepancy

Fig. 3.1 shows a subset of data taken during Period 2 with each species's expectation curve overlaid. By visual inspection, it's clear that the pion and electron data fall about a nanosecond earlier than expected. This is the time of flight discrepancy this study characterizes and attempts to diagnose.

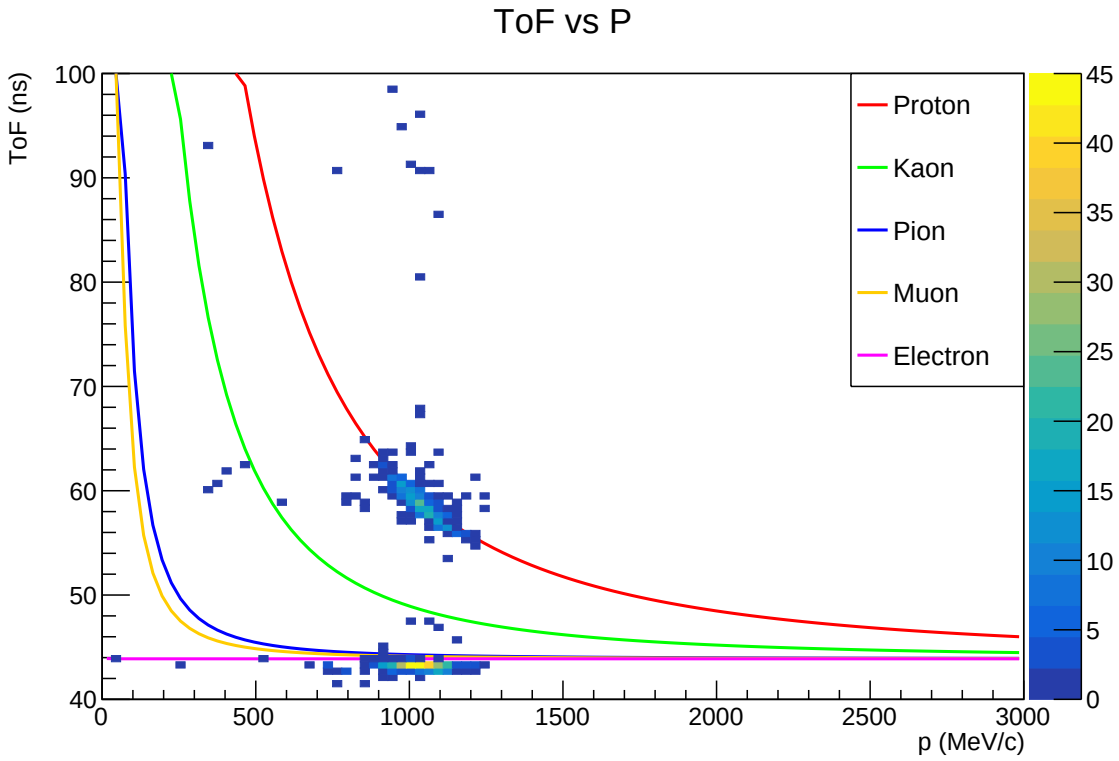

Figure 3.1: A subset of data taken during Period 2 (pre-redeployment) in phase space with each species's expectation curve overlaid as described in Sec. 2.1.

The selection criteria for each species are noted in Tab. 3.1.

Figs. 3.2, 3.3, and 3.4 show the percent difference between the data and expectation for each species's time of flight for the momentum range of interest. The protons average a 0.54% difference, the pions a 2.47% difference, and the electrons a 2.89% difference in time of flight.

In the following subsections I consider two hypotheses of the cause of the time of flight discrepancy.

This is the strategy: under the assumption of each hypothesis, all species' expectation curves are transformed such that the pion expectation curve pierces the pion data peak, calculated at (1022.22 MeV/c, 43.2379 ns). Then the hypothesis is evaluated based on how well its transformation matches the proton expectation curve

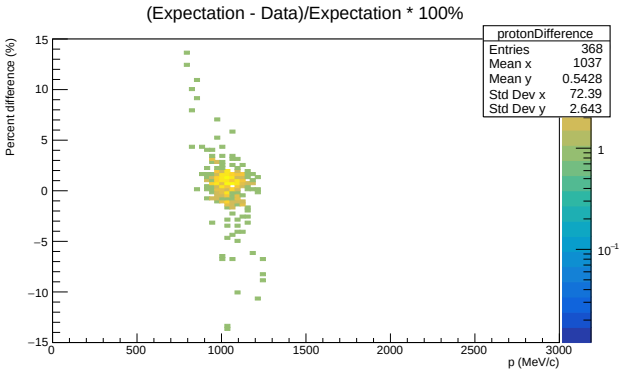

Figure 3.2: Percent difference between data and expectation for time of flight for protons.

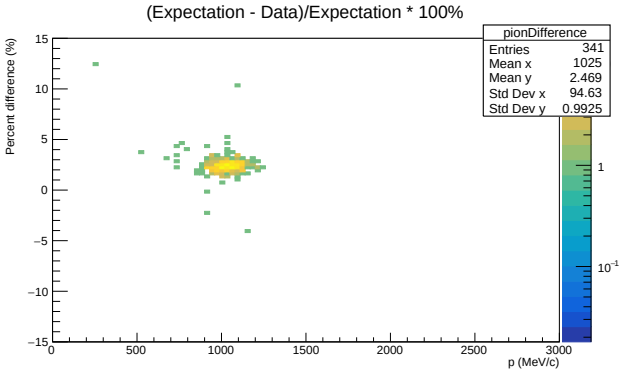

Figure 3.3: Percent difference between data and expectation for time of flight for pions.

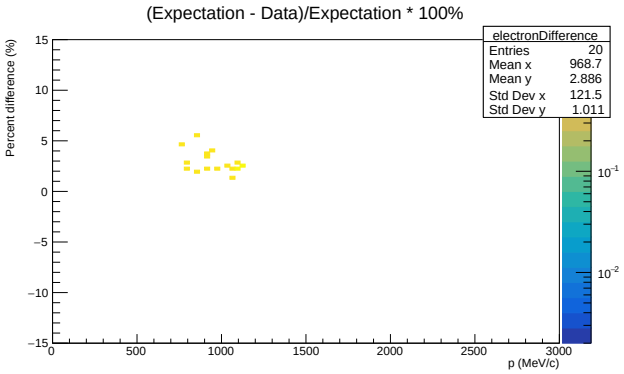

Figure 3.4: Percent difference between data and expectation for time of flight for electrons.

Protons	54 ns $\leq ToF$ and 400 MeV/$c \leq p$
Pions	$ToF \leq$ 46 ns and Cherenkov not triggered
Electrons	Cherenkov triggered

Table 3.1: The selection criteria for each particle species determined by eye, pre-redeployment, using the DS-PMT as the downstream detector. Deuterons (whose expectation curves are not drawn), kaons, and muons are not considered due to their low turnout in the data.

to the proton data. The pathlength is considered to be 13.15639 m [7],[1] a value that ignores the curved paths particles take within the magnet and any small differences in pathlength due to differently angled particle trajectories.

[1] Considering this many digits may not be justified from a significant figures perspective. However, this value was reported to me by a collaborator, and I used it for the sake of maintaining consistency across projects.

3.1 The Source of the Discrepancy

3.1.1 Hypothesis: A misunderstanding of the time of flight reconstruction

See Sec. 2.3 for a discussion of the time of flight reconstruction. If the misunderstanding causes a uniform (independent of momentum) shift in the reconstructed time of flight, the difference can be calibrated out by some constant shift in the expectation curves. At the momentum of the pion data peak, the expectation curves must be shifted down 1.0281 ns to match the pion time of flight expectation to the data. This shift results in the phase space shown in Fig. 3.5 and the percent difference plots shown in Figs. 3.6, 3.7, and 3.8.

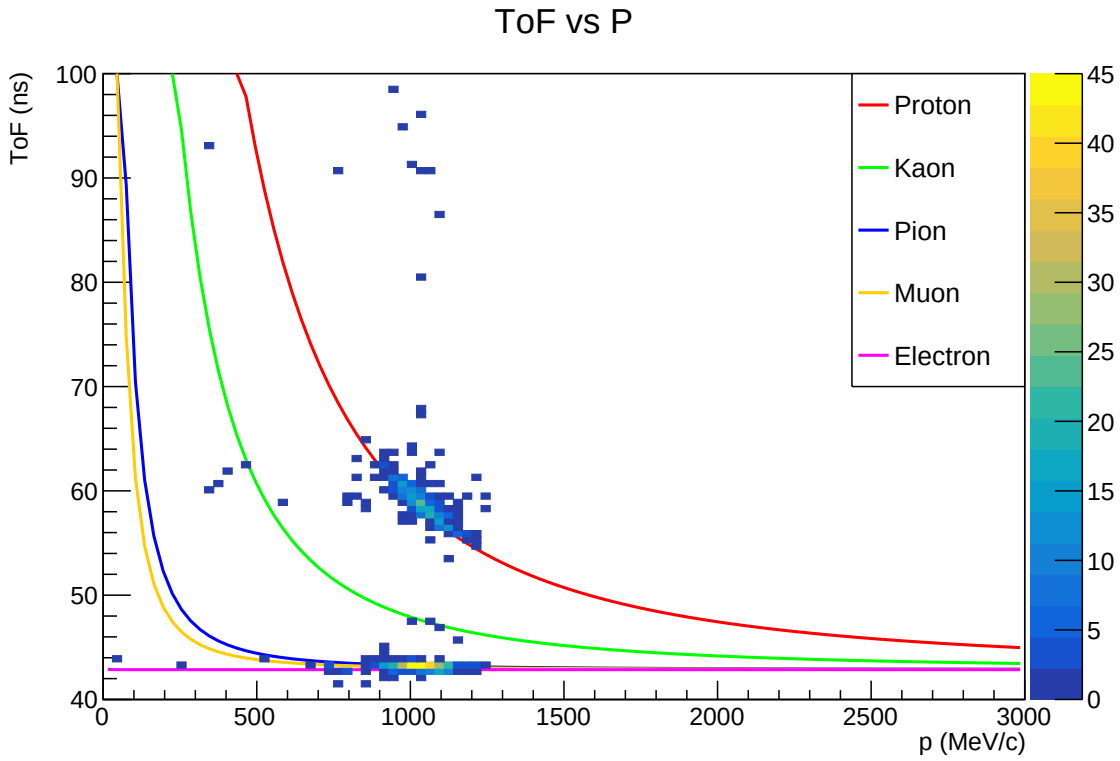

Figure 3.5: A subset of data taken during Period 2 (pre-redeployment) in phase space with each species's expectation curve overlaid as described in Sec. 2.1 after the time of flight shift described in Sec. 3.1.1.

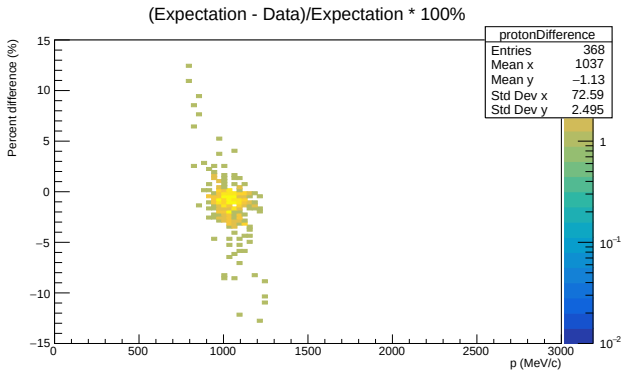

Figure 3.6: Percent difference between data and expectation for time of flight for protons after the time of flight shift described in Sec. 3.1.1.

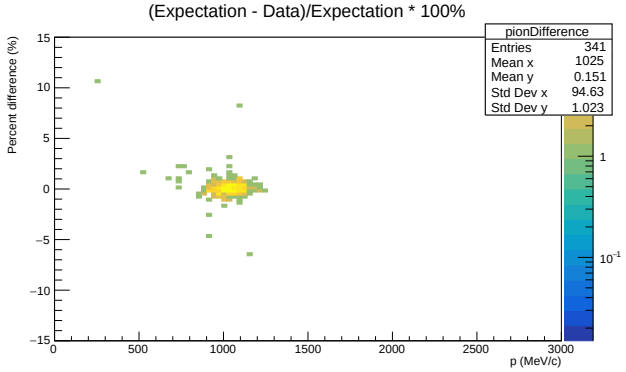

Figure 3.7: Percent difference between data and expectation for time of flight for pions after the time of flight shift described in Sec. 3.1.1.

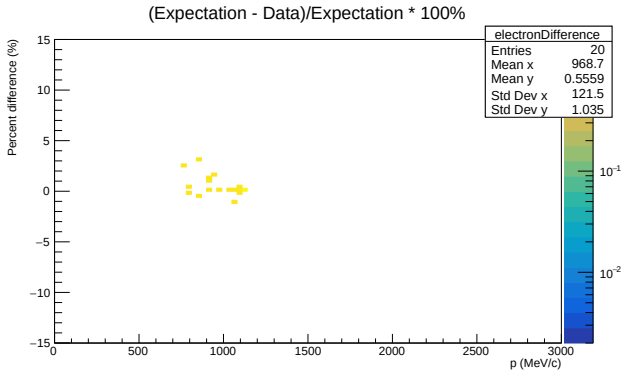

Figure 3.8: Percent difference between data and expectation for time of flight for electrons after the time of flight shift described in Sec. 3.1.1.

3.1.2 Hypothesis: A misunderstanding of the pathlength

If the pathlength (d in Eq. 2.1, reproduced below) is misunderstood, the difference can be calibrated out by scaling the time of flight by some factor. At the momentum of the pion data peak, the expectation curves must be scaled down by a factor that corresponds to a pathlength reduction of 30.56 cm to match the pion time of flight expectation to the data. This scaling results in the phase space shown in Fig. 3.9 and the percent difference plots shown in Figs. 3.10, 3.11, and 3.12.

$$ToF(p) = d\sqrt{\frac{m^2}{p^2} + \frac{1}{c^2}}$$

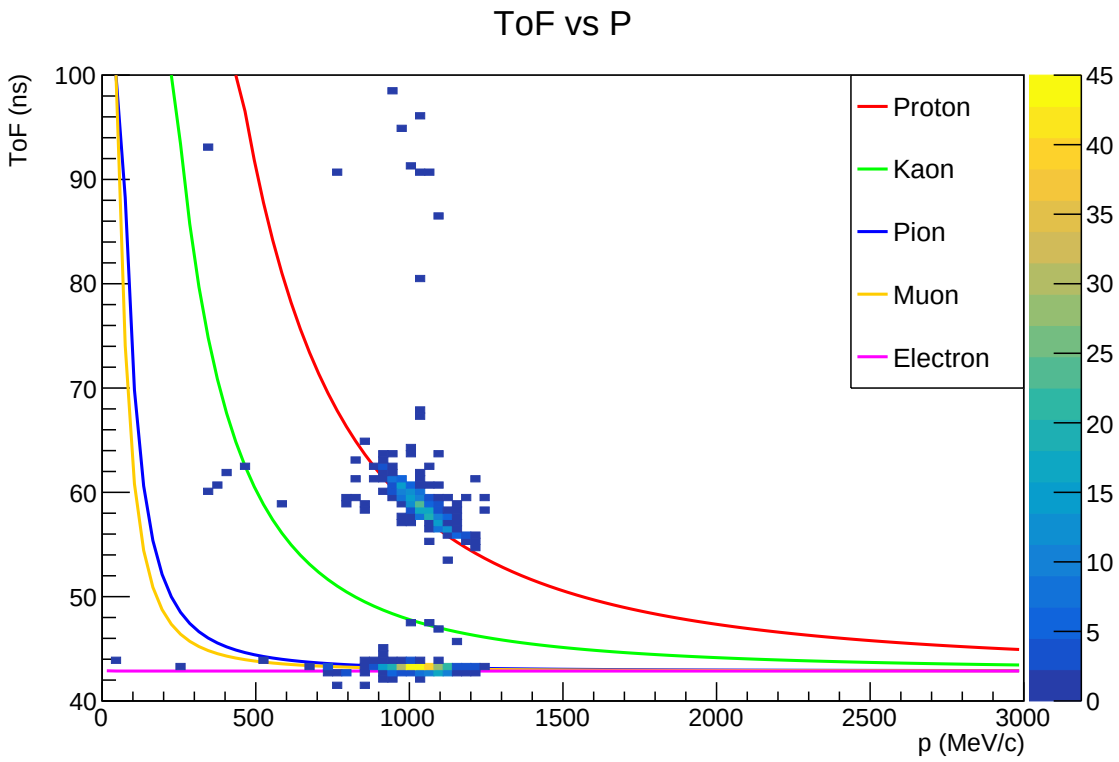

Figure 3.9: A subset of data taken during Period 2 (pre-redeployment) in phase space with each species's expectation curve overlaid as described in Sec. 2.1 after the pathlength shift described in Sec. 3.1.2.

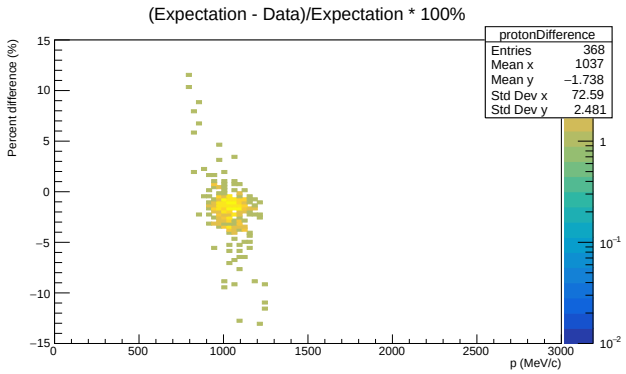

Figure 3.10: Percent difference between data and expectation for time of flight for protons after the pathlength shift described in Sec. 3.1.2.

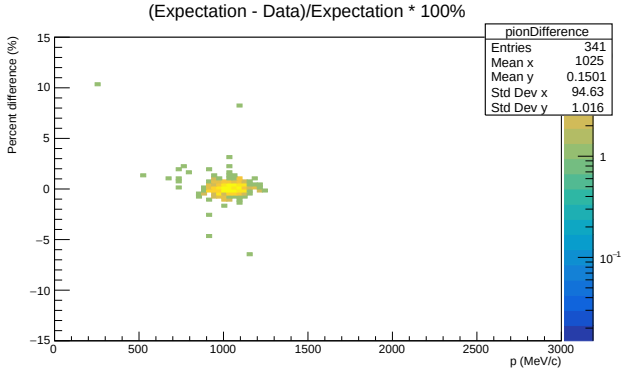

Figure 3.11: Percent difference between data and expectation for time of flight for pions after the pathlength shift described in Sec. 3.1.2.

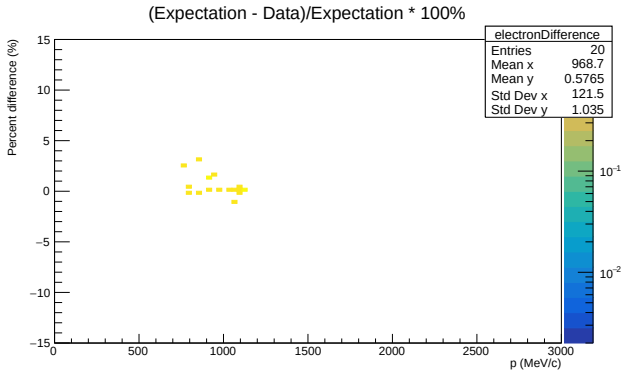

Figure 3.12: Percent difference between data and expectation for time of flight for electrons after the pathlength shift described in Sec. 3.1.2.

3.2 Results

Under the hypothesis that the time of flight reconstruction is misunderstood (Sec. 3.1.1), the relevant shift of the expectation curves exacerbates the proton expectation curve's average percent difference from the data from 0.54% to -1.13%. Under the hypothesis that the pathlength measurement is misunderstood (Sec. 3.1.2), the relevant scaling of the expectation curves similarly exacerbates the proton expectation curve's average percent difference from the data from 0.54% to -1.74%.

Therefore, for neither hypothesis considered does this analysis show an improved agreement with data. However, time slew is an effect that may prove confounding. I've included a basic discussion of the phenomenon and a possible approach to addressing it in a similar study in Appendix A.

3.3 Conclusion

At this point in my study, the ToF detectors were redeployed (see Chap. 4). Plotting a subset of data in phase space using the DS-PMT in its new location as the downstream detector and comparing to expectation curves (Fig. 3.13), under the assumption of a 9.70772 m pathlength (calculated from survey values and again ignoring the curved paths particles take within the magnet and any small differences in pathlength due to differently angled particle trajectories), it's clear by visual inspection that the discrepancy is no longer present. The cause of the discrepancy remains unknown at the time of writing, and it may be worthwhile for a future collaborator to continue this study for the sake of improving our understanding of the pre-redeployment data.

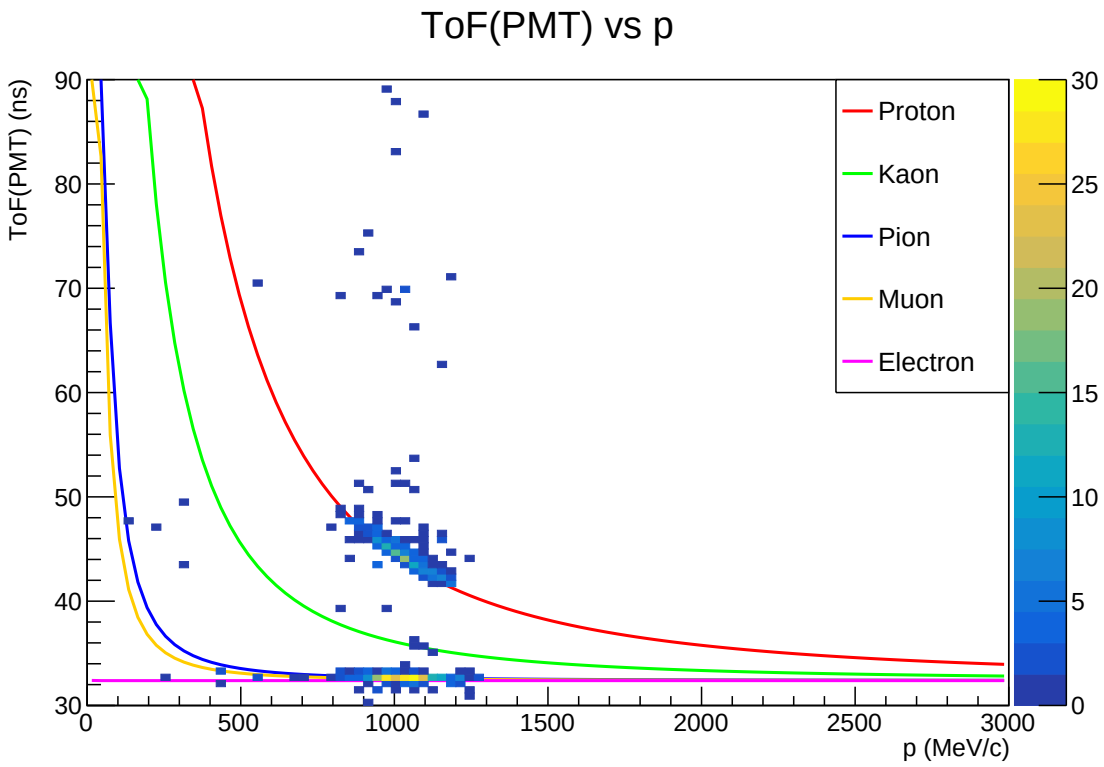

Figure 3.13: A subset of data taken during Period 3 (post-redeployment) in phase space using DS-PMT as the downstream arm with each species's expectation curve overlaid as described in Sec. 2.1.

Chapter 4

Redeployment

On December 10, 2020, the DS-PMT and the US-PMT detectors were moved to new locations. The original configuration of the detectors is shown in Fig. 4.1, and the redeployed configuration is shown in Fig. 4.2.

Figure 4.1: The pre-redeployment configuration of the ToF detectors. TOFc is the time it would take light to travel the indicated pathlength, to be interpreted as an estimate of the time of flight of fast particles. Slide: Alex Sousa, docdb-48480

The redeployment was intended to increase the beamline's geometric acceptance, which is the proportion of particles that pass through the beamline whose times of flight can be reconstructed (as a function of the beamline's geometry). See Appendix B for further discussion.

Figure 4.2: The post-redeployment configuration of the ToF detectors. TOFc is the time it would take light to travel the indicated pathlength, to be interpreted as an estimate of the time of flight of fast particles. Slide: Alex Sousa, docdb-48480

For this project, it was prudent to investigate the timing data from the detectors' new positions. As discussed in Sec. 3.3, the US-PMT→DS-PMT data showed an increase in agreement with expectations and the arm was ready to be used for particle ID after a precise survey of the detectors' new positions. We were additionally interested in analyzing data from the SiPM detector, which prior to the redeployment had not been given a role in reconstruction. Our aim was to introduce the SiPM detector as the downstream detector for a new time of flight arm, so that for every particle that triggered the relevant detectors two times of flight could be reconstructed (using both the US-PMT→DS-PMT arm and the US-PMT→SiPM arm).

Chapter 5

Second Study: Post-redeployment SiPM Calibration

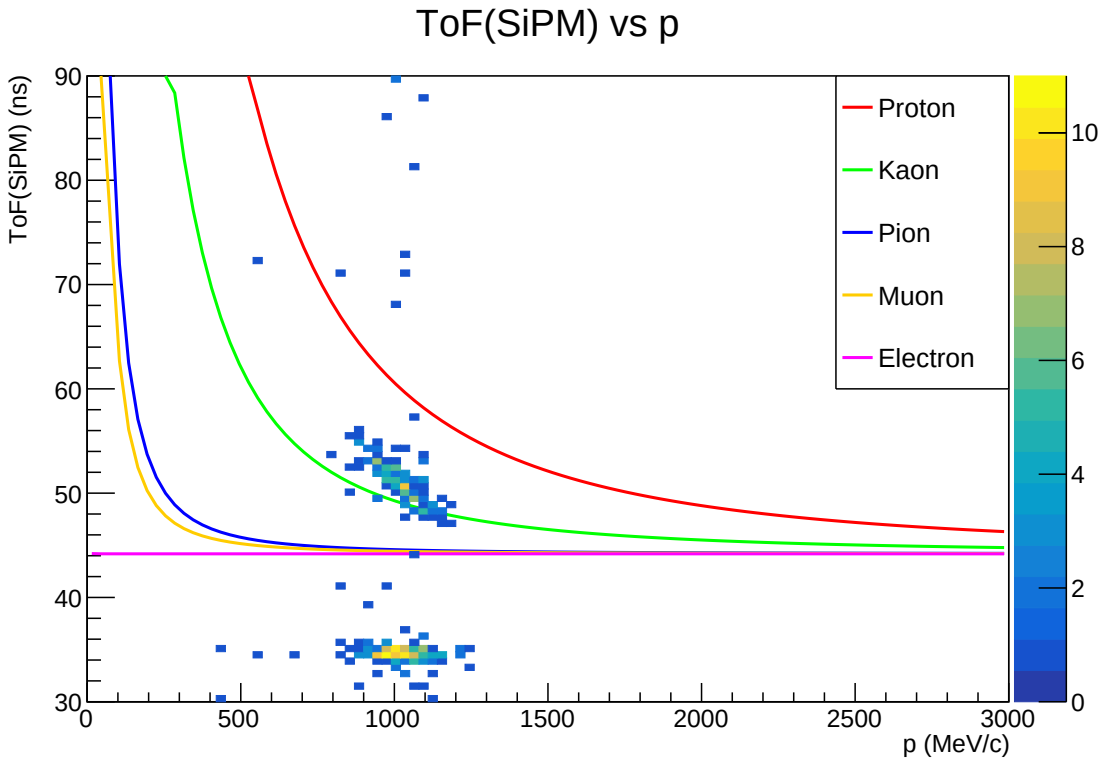

Figure 5.1: A subset of data taken during Period 3 (post-redeployment) in phase space using the SiPM as the downstream arm with each species's expectation curve overlaid as described in Sec. 2.1.

Fig. 5.1 compares the post-redeployment SiPM data with expectation, under the

assumption of a 13.2455 m pathlength (calculated from survey values and again ignoring the curved paths particles take within the magnet and any small differences in pathlength due to differently angled particle trajectories). Clearly, there is a significant difference between the two. This second study attempts to understand the discrepancy and calibrate it out so that the SiPM can be used for time of flight reconstruction, and therefore particle ID.

5.1 The Source of the Discrepancy

5.1.1 Hypothesis: A misunderstanding of the reconstruction algorithm

The time of flight reconstruction algorithm is described in Sec. 2.3. As a refresher, for each time of flight paddle, the paddle's hit time is calculated as either the earliest or the average of each of the paddle's PMTs' hit times. Each PMT's hit time is determined by constant fraction discrimination, described in Appendix A. We know that the DS-PMT's reconstruction leads to results that match our expectations (see Fig. 3.13), so we can use its behavior as a basis for comparison for the SiPM's. The scope trace for the downstream detectors for an arbitrary event is shown in Fig. 5.2 and one of the SiPM's channels' scope trace's for the same event is isolated in Fig. 5.3.

The DS-PMT's reconstruction assigns hit times that line up with the beginnings of pulses, so if a misunderstanding of the reconstruction algorithm were contributing to the discrepancy, we would expect to see the algorithm assign hit times to the SiPM that do not line up with beginnings of pulses. The discrepancy is around 10 ns, which is 25 digitizer ticks, or 5 marks along the x-axis in Figs. 5.2 and 5.3. But by visual inspection the reconstruction places the SiPM's hit time at the start of the pulse, or at least close enough that a discrepancy on the order of 10 ns cannot

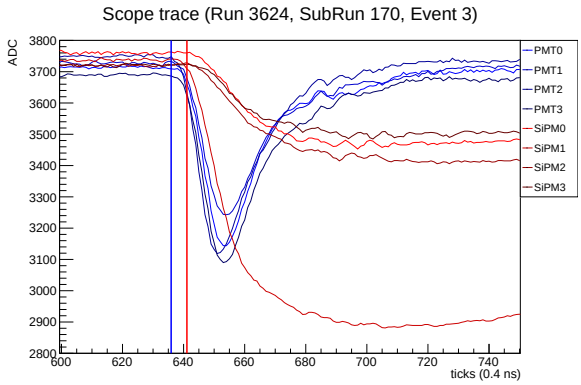

Figure 5.2: The scope trace from the downstream detectors for an arbitrary event. Each vertical line indicates the hit time for each paddle as determined by the time of flight reconstruction algorithm.

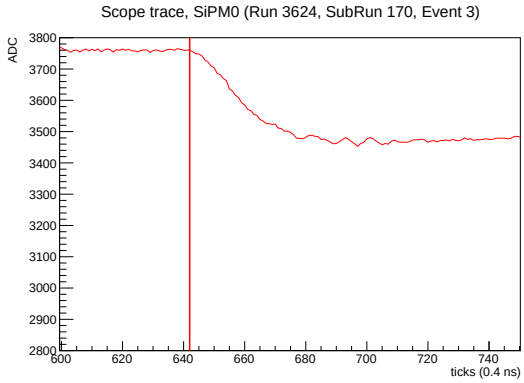

Figure 5.3: The scope trace from one of the SiPM's channels for an arbitrary event. The vertical line indicates the hit time for the channel as determined by the time of flight reconstruction algorithm.

be seen. Therefore any misunderstanding of the reconstruction algorithm does not significantly contribute to the discrepancy.

5.1.2 Hypothesis: A series of delays

The investigations for this hypothesis were not done by me, but I briefly describe them here for the sake of completeness.

Mike Wallbank and Yağmur Torun measured the calibration of the digitizer channels and did not find a source of the discrepancy. [8]

In an email exchange initiated by Mike Wallbank, Steven Block of the University of Dallas proposed a new explanation for the discrepancy: a series of previously unaccounted-for delays. He estimated that the internal delay a signal experiences when it travels through the US-PMT likely contributes ∼5.8 ns, the pigtail cables from the US-PMT likely contribute ∼7.5 ns, and internal delays within the SiPM oppose those contributions by ∼1 ns. Summing these estimates yields $5.8 + 7.5 - 1$ ns = 10-12 ns, matching the observed discrepancy. The delays due to the US-PMT had not previously been considered because they were known to nearly offset equivalent delays due to the DS-PMT in the US-PMT→DS-PMT time of flight arm. It's sensible to think that we were only noticing these delays now because it was the first time we were attempting to use the SiPM as a detector in a time of flight arm. [9]

After the current (as of May 9, 2021) run of data collection, the Test Beam group will perform a standard calibration of the US-PMT and SiPM detectors to properly measure these delays for use in analysis.

5.2 Calibrating out the SiPM Discrepancy

The mechanism causing the SiPM discrepancy does not need to be fully understood to begin data analysis with the arm using a temporary method for calibration. Two methods of calibration were already prepared for this project's first study: the application of a uniform time of flight shift to the data, and the application of a uniform pathlength shift to the data. To compare these methods to determine which is more suitable, I use the strategy described in Ch. 3: under each method, I shift the pion expectation curve to match the pion data peak and then compare the proton data to the shifted proton expectation curve.

For the time of flight shift method, at the momentum of the pion data peak, calculated at (1018 MeV/c, 34.62 ns), the expectation curves must be shifted down

9.9489 ns to match the pion time of flight expectation to the data. This shift results in the phase space shown in Fig. 5.4 and the percent difference plot for protons shown in Fig. 5.5.

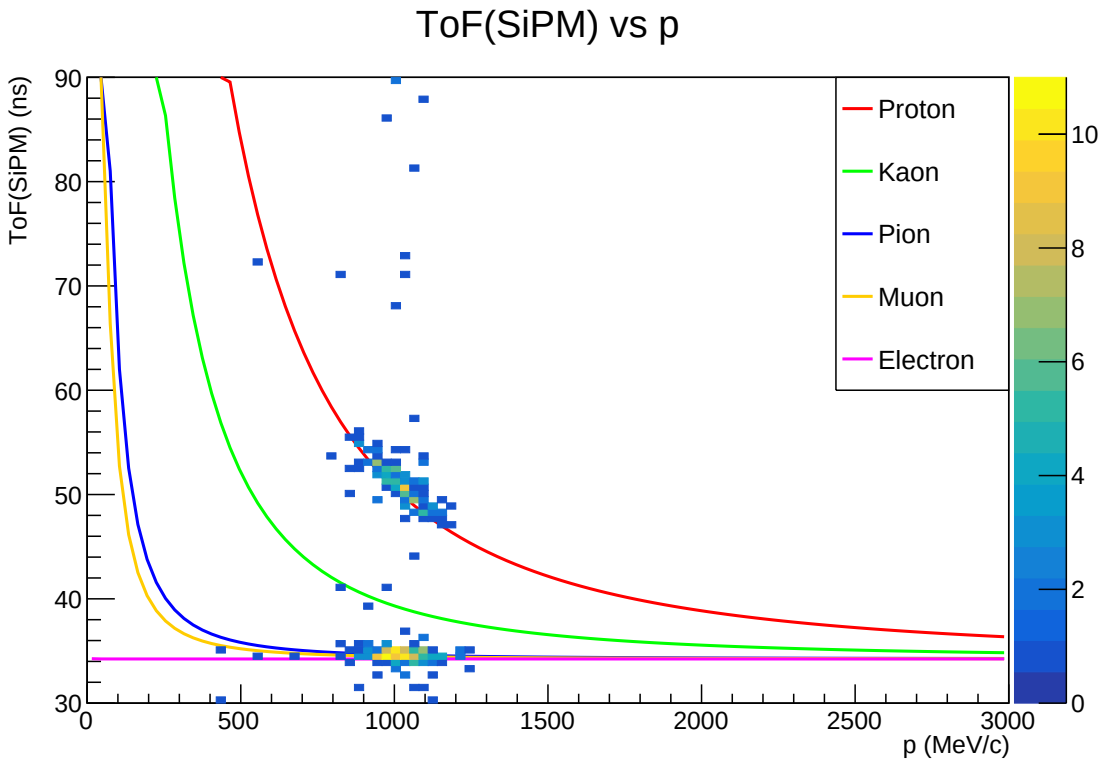

Figure 5.4: A subset of data taken during Period 3 (post-redeployment) in phase space using the SiPM as the downstream arm with each species's expectation curve overlaid as described in Sec. 2.1 after the time of flight shift described in Sec. 5.2.

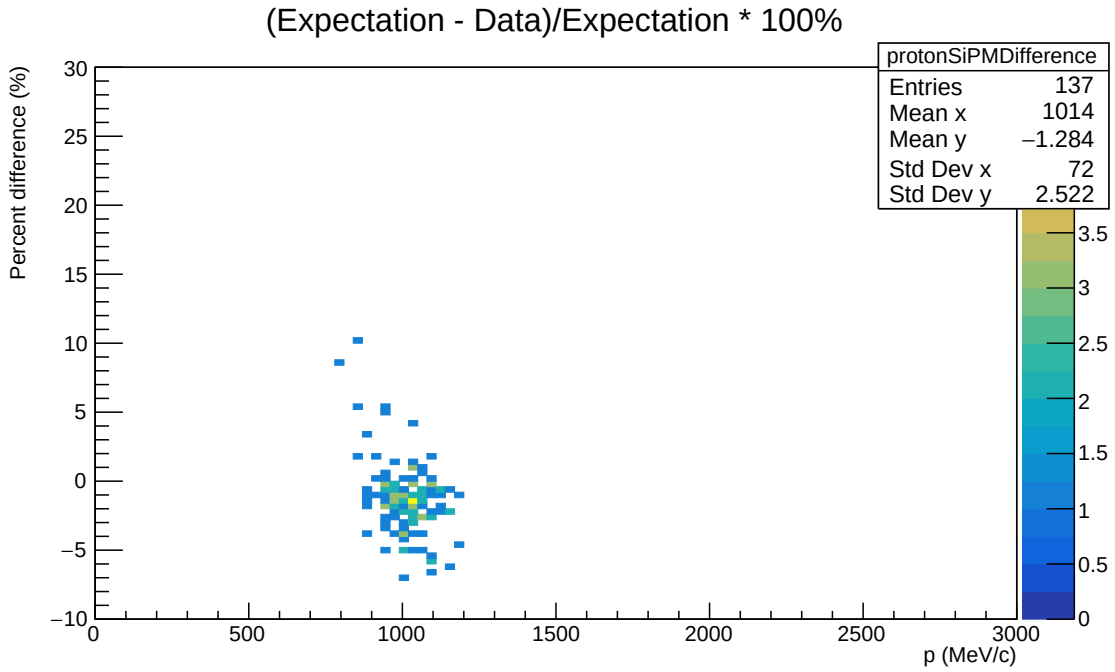

Figure 5.5: Percent difference between data and expectation for time of flight for protons after the time of flight shift described in Sec. 5.2, using the SiPM as the downstream arm.

For the pathlength shift method, at the momentum of the pion data peak, the expectation curves must be scaled down by a factor that corresponds to a pathlength reduction of 2.9555 m to match the pion time of flight expectation to the data. This scaling results in the phase space shown in Fig. 5.6 and the percent difference plot for protons shown in Fig. 5.7.

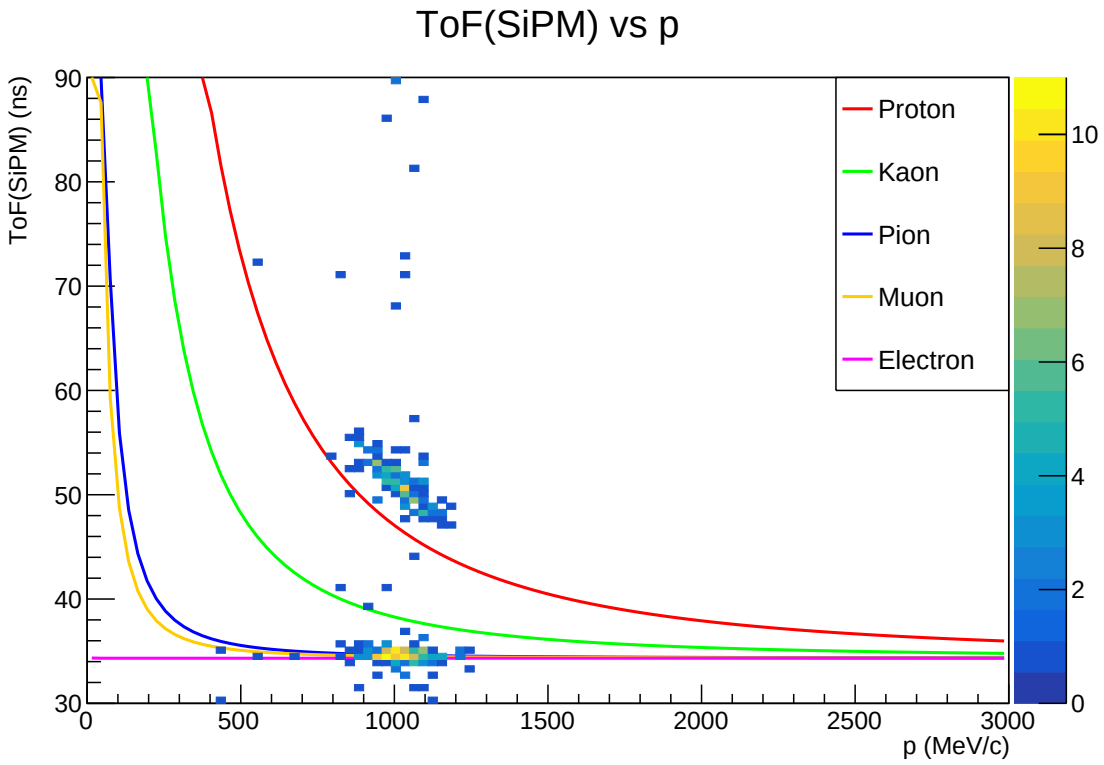

Figure 5.6: A subset of data taken during Period 3 (post-redeployment) in phase space using the SiPM as the downstream arm with each species's expectation curve overlaid as described in Sec. 2.1 after the pathlength shift described in Sec. 5.2.

Using the pathlength shift method, matching the pion expectation curve to the pion data peak causes the proton expectation curve to far overshoot the proton data. Using the time of flight shift method, matching the pion expectation curve to the pion data peak causes the proton expectation curve to reasonably approximate the proton data, and the percent difference between the proton expectation and data is reasonably flat across the momentum range of interest. Therefore, some constant time of flight shift can be reasonably used as a method to calibrate out the discrepancy before a standard calibration is conducted.

To find the shift value as accurately as possible, I plotted the entire existing post-redeployment dataset (as of April 13, 2021), selected the electrons — which are more

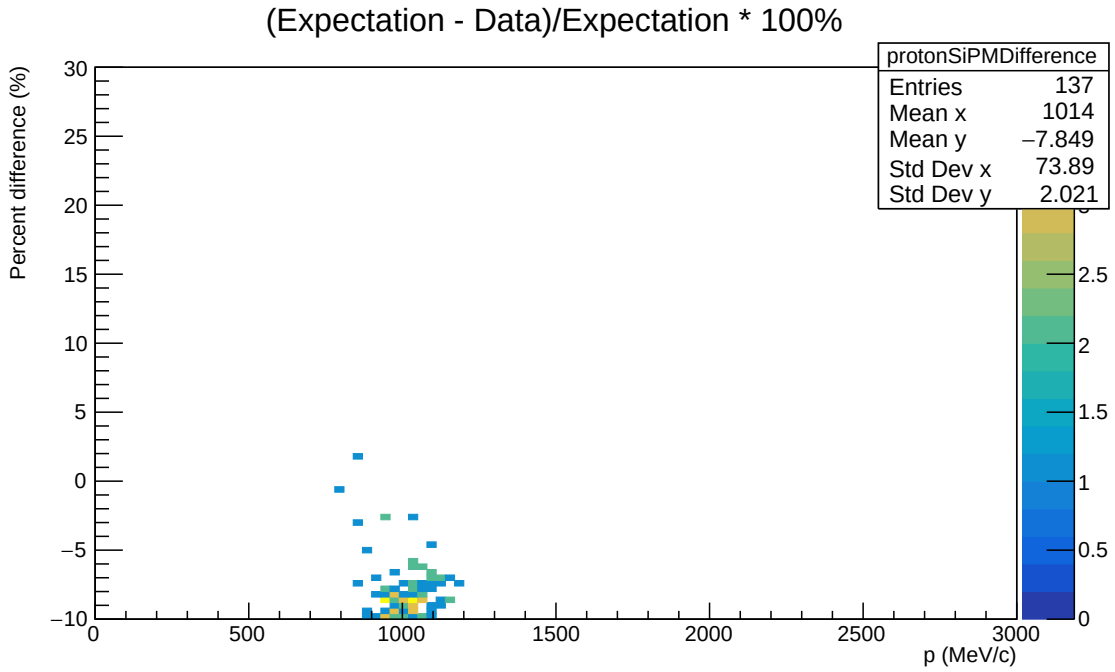

Figure 5.7: Percent difference between data and expectation for time of flight for protons after the pathlength shift described in Sec. 5.2, using the SiPM as the downstream arm.

definitively tagged than pions, as described in Sec. 2.4, and provide usable statistics in this larger sample size — and performed a Gaussian fit on each axis of phase space to identify the electron data peak. The phase space including all events is shown in Fig. 5.9, the selected electrons are shown in Fig. 5.10, the momentum fit is shown in Fig. 5.11, and the time of flight fit is shown in Fig. 5.12.

There is some nuance in selecting electrons from phase space data. It's reasonable to think that the only cut on the data that would be necessary to select electrons is the Cherenkov cut, because a hit in the Cherenkov detector definitively tags electrons. However, applying only the Cherenkov cut yields additional strips of events at intervals of 19 ns above the strip of data that correspond to electrons at a reasonable time of flight (given the pathlength and the discrepancy), as shown in Fig. 5.8. The difference in time between these strips of unwanted events corresponds to the beam's

bucket size of 19 ns. What's happening is that a particle from one bucket is triggering the upstream detector and within the same event a particle from another bucket is triggering the downstream detector, giving the illusion of a single particle with a time of flight greater by an integer multiple of 19 ns. [10] Therefore, electrons were identified with events with a triggered Cherenkov detector and with reconstructed times of flight less than or equal to 42 ns, a value determined by eye.

From the fit, the electron data peak is calculated at (1021.39 MeV/c, 34.1077 ns), and the time shift value for use in calibration before the standard calibration procedure is conducted is calculated at 10.0745 ns.

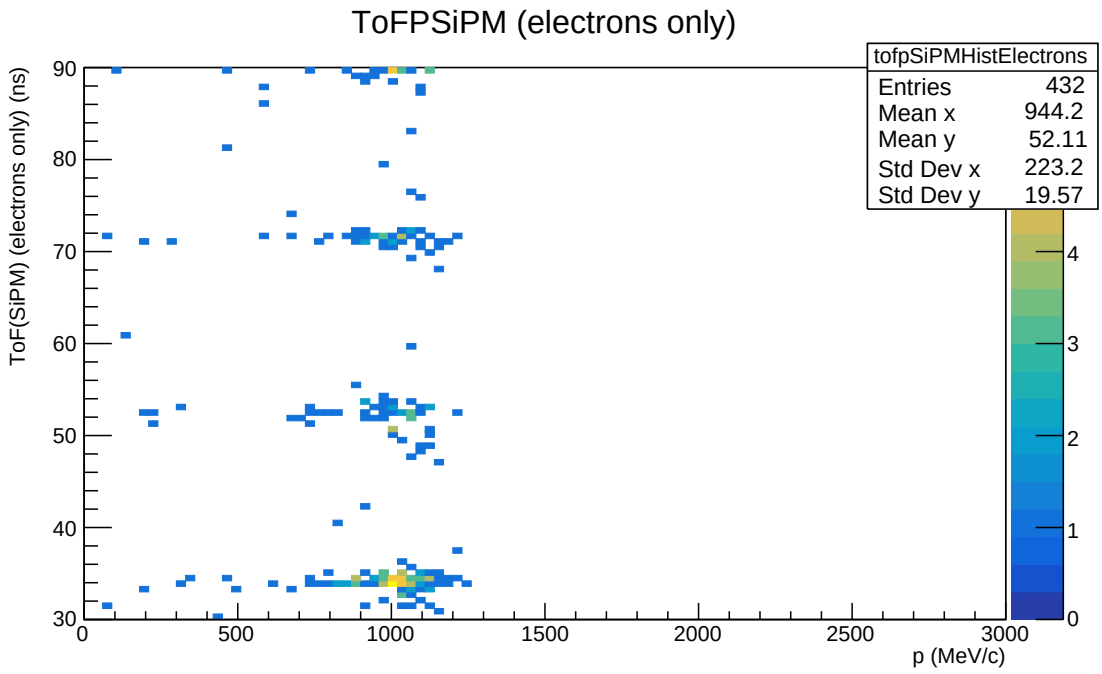

Figure 5.8: Some events after the Cherenkov cut and before a time of flight cut, to illustrate the 19 ns bucket size of the beam as described in the footnote in Sec. 5.2.

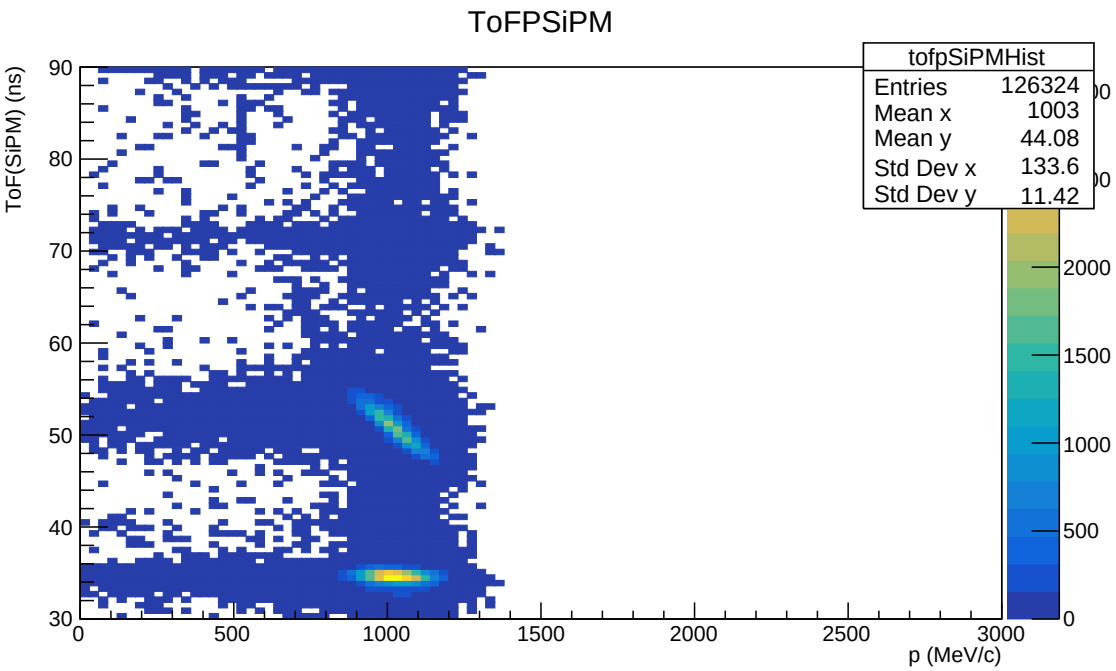

Figure 5.9: A larger subset of data taken during Period 3 (post-redeployment) in phase space using the SiPM as the downstream arm.

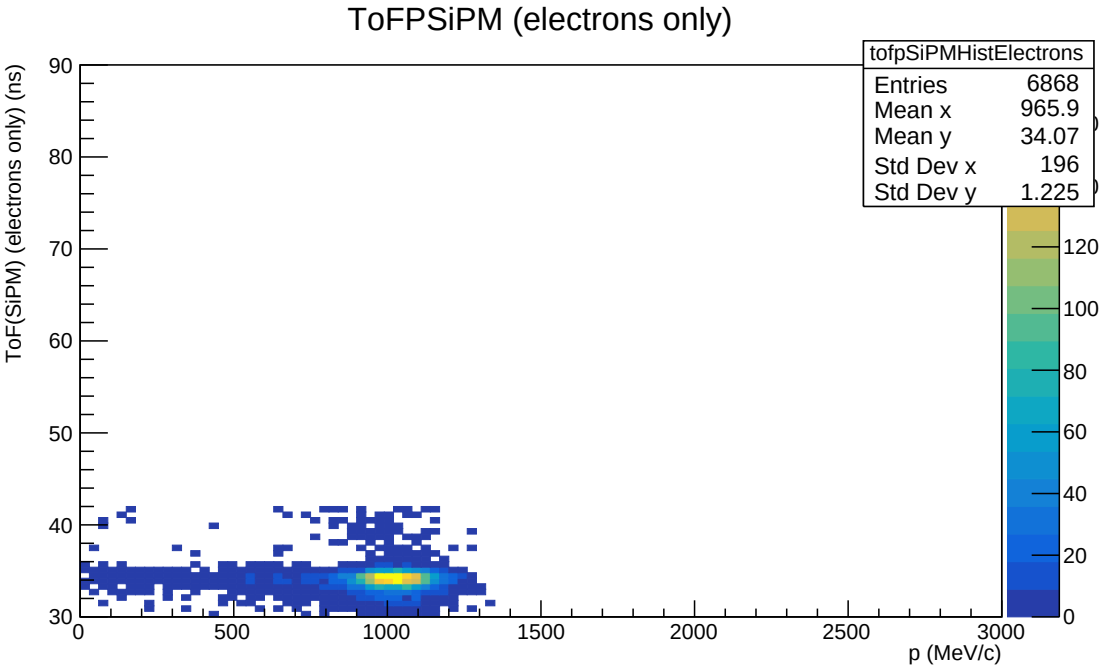

Figure 5.10: A larger subset of data taken during Period 3 (post-redeployment) in phase space using the SiPM as the downstream arm, selecting electrons.

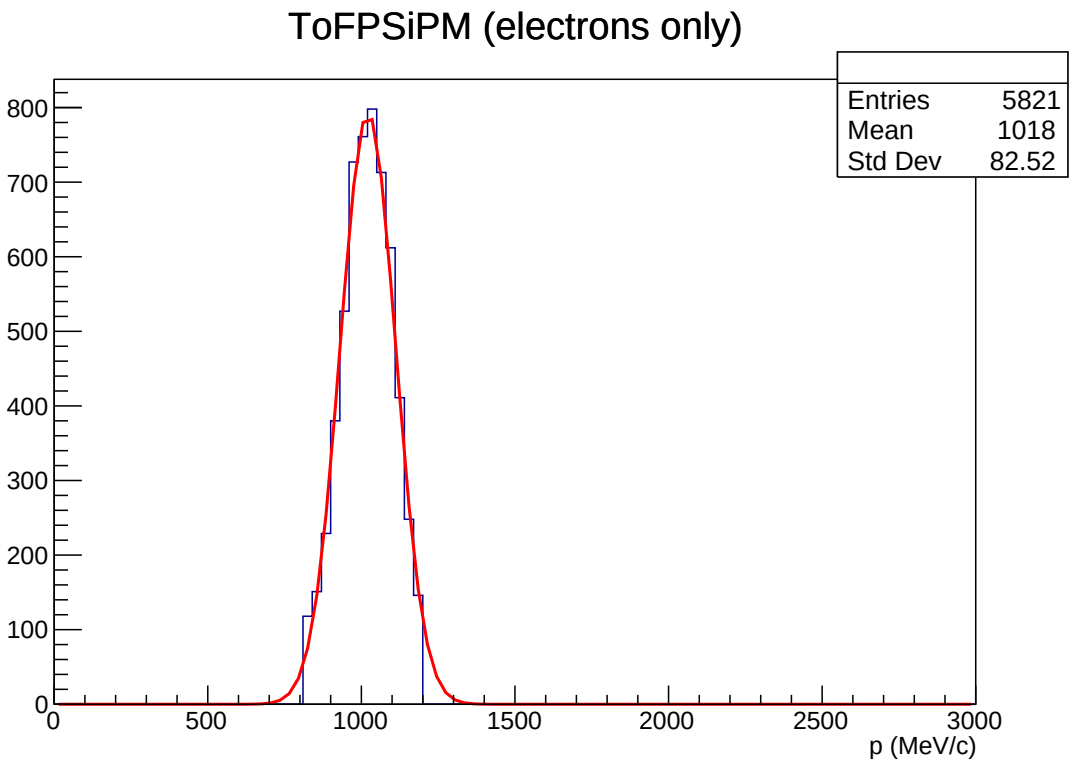

Figure 5.11: A Gaussian fit of the reconstructed momentum of the selected electrons.

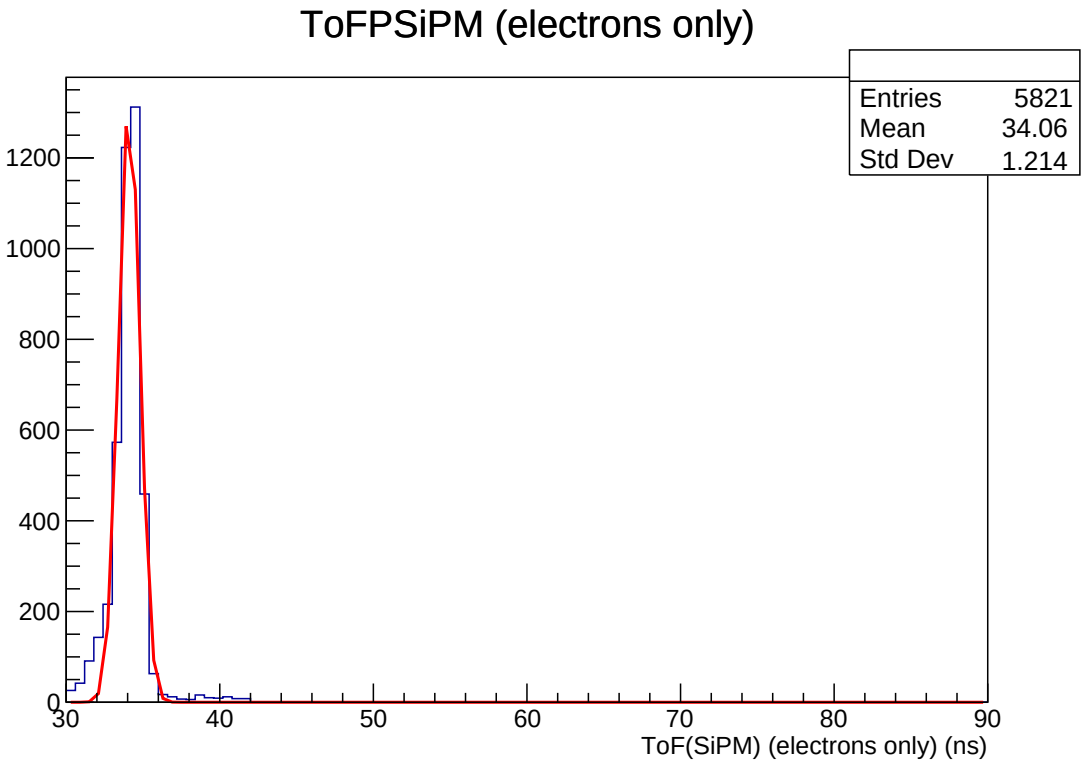

Figure 5.12: A Gaussian fit of the reconstructed time of flight of the selected electrons.

Chapter 6

Conclusion

Originally, the goal of this project was to diagnose the ∼2 ns discrepancy in the time of flight data in the Test Beam time of flight system. While neither hypothesis investigated proved promising and the discrepancy remains unexplained, conducting the first study on the ∼2 ns discrepancy allowed for a more efficient second study on the ∼10 ns discrepancy because by the time of the redeployment, I understood the methodology for comparing time of flight data with expectations and had written the code to do so. The calibration value I found, 10.0745 ns, allows for the use of the SiPM as the downstream detector in a new time of flight arm. A more accurate calibration value will be determined in the future by direct study of the SiPM's electronics.

Appendix A

Time Slew and Constant Fraction Discrimination

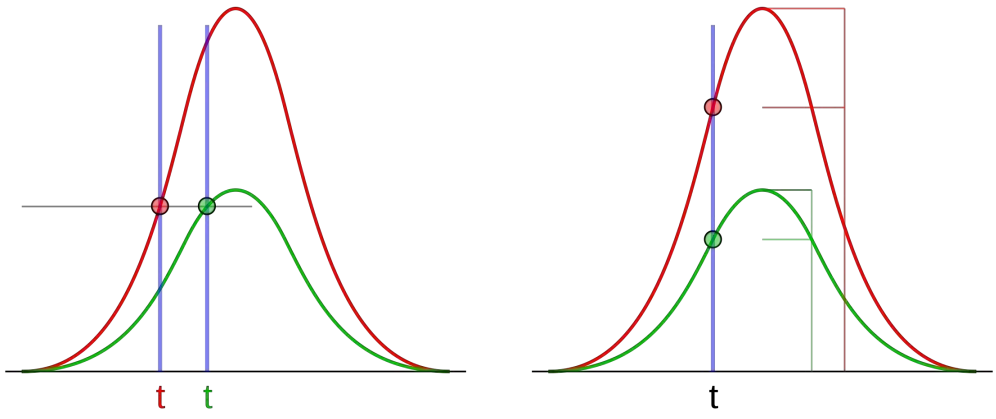

Figure A.1: Left: the threshold method for determining hit time. Right: the constant fraction discrimination method for determining hit time, assuming equal rise times. Image: Wikipedia

Time slew is an artifact of the fact that time-to-digital converters (TDCs) read out signals that are spread out in time. It's necessary to implement a strategy to reconstruct a standardized hit time from these spread out signals.

One strategy is to define a threshold charge: a TDC defines the hit time as the time it reads out a certain charge value. But there is a problem with the threshold

strategy: two pulses of different amplitudes but whose peaks align in time will give different hit times (see the left diagram in Fig. A.1).

A solution to this problem is an alternate strategy called constant fraction discrimination (and the device that performs it is called a constant fraction discriminator, or CFD). For every pulse, a CFD defines a threshold that is a constant fraction of that pulse's amplitude. Therefore, a CFD that encounters two pulses of different amplitude but whose peaks align in time will determine identical hit times, provided that both pulses have identical rise times (see the right diagram in Fig. A.1).

The Test Beam's analysis uses the CFD strategy, but if a time slew were nonetheless identified, it could help explain the pre-redeployment time of flight discrepancy. Before the redeployment, I'd planned to investigate this path by comparing hit times determined by each PMT in each time of flight paddle over a range of signal amplitudes. [11]

Appendix B

Geometric Acceptance and Redeployment

By comparing the fraction of events that pass time of flight reconstruction between runs pre-redeployment and runs post-redeployment, we can assess whether the redeployment increased the beam's geometric acceptance as anticipated. This evaluation is incomplete, but included anyway for the sake of a potential future project.

To evaluate the increase in acceptance we expect from the redeployment, we need to understand the geometry of the beamline. The time of flight paddles are each 5.9 by 5.9 inches, and the wire chambers are each 5 by 5 inches. Before the redeployment, acceptance was limited by the former downstream time of flight paddle, which was 575 inches from the target (along the beamline, which changes direction in the magnet). After the redeployment, acceptance is limited by the closest wire chamber to the detector, 406 inches from the target. [12] [13]

Because the wire chambers and time of flight paddles are squares, we can find the solid angle they cover from the perspective of the target by squaring the one-

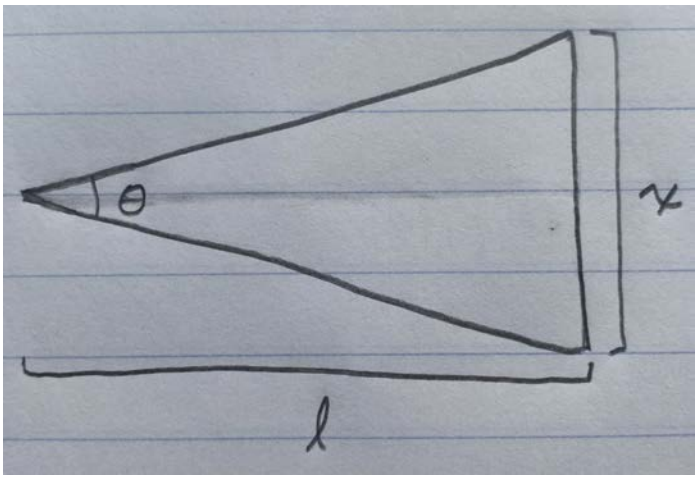

Figure B.1: Geometry reference for the geometric acceptance calculation

dimensional angle they subtend. See Fig. B.1 for a reference.

$$\begin{aligned}
\tan\theta/2 &= \frac{x/2}{l} = \frac{x}{2l} \\
\theta/2 &= \arctan\frac{x}{2l} \\
\theta &= 2\arctan\frac{x}{2l} \\
\theta^2 &= 4\arctan^2\frac{x}{2l}
\end{aligned}$$

Pre-redeployment, $x = 5.9$ inches and $l = 575$ inches, so $\theta^2 = 105.284 \times 10^{-6}$ steradians. Post-redeployment, $x = 5$ inches and $l = 406$ inches, so $\theta^2 = 151.662 \times 10^{-6}$ steradians. Taking the ratio between the two, we'd expect that the redeployment increased the angular acceptance by around 44%.

Tab. B.1 shows a sample of the the cut flow pre-redeployment, and Tab. B.2 shows a sample of the cut flow post-redeployment. SiPM data is omitted from the pre-redeployment table because its data was not included in reconstructed files pre-redeployment.

Due to the extremely low percentage of events that reportedly pass momentum reconstruction pre-redeployment, I believe the method by which I constructed the cut flow for the pre-redeployment data is flawed, and therefore it would be unreasonable to

Total number of events considered:		795	100%
Number of events that passed:	momentum	39	5%
	PMT ToF	771	97%
	momentum and PMT ToF	39	5%

Table B.1: A sample of the cut flow pre-redeployment. There's likely a flaw in the way this table was constructed, and the values are included only for reference within this report.

Total number of events considered:		2186	100%
Number of events that passed:	momentum	1462	67%
	PMT ToF	1886	86%
	momentum and PMT ToF	1359	62%
	SiPM ToF	1117	51%
	momentum and SiPM ToF	870	40%
	both ToF	1110	51%
	momentum and both ToF	866	40%

Table B.2: A sample of the cut flow post-redeployment.

use Tab. B.1 in evaluation of the redeployment's increase of geometrical acceptance. Then, as with the analysis of the time slew, I'll recommend further investigation to a future collaborator.

Appendix C

Event Displays

These are event displays for an arbitrary selection of post-redeployment events identified using the US-TOF→SiPM time of flight arm. The selection criteria are listed in Tab. C.1. Included are event displays for five protons, five pions or muons, and five electrons.

Protons	$41 \leq ToF \leq 56$ ns and Cherenkov not triggered
Pions or Muons	$ToF \leq 38$ ns and Cherenkov not triggered
Electrons	$ToF \leq 38$ ns and Cherenkov triggered

Table C.1: The selection criteria for each particle species determined by eye, post-redeployment, using the SiPM as the downstream detector.

Frequently, more than one particle appears in an event display. Most coincident particles also come from the beam, and some come from cosmic rays. Often, considering only the data around 50 μs into the event isolates the particle that triggered the event. [14]

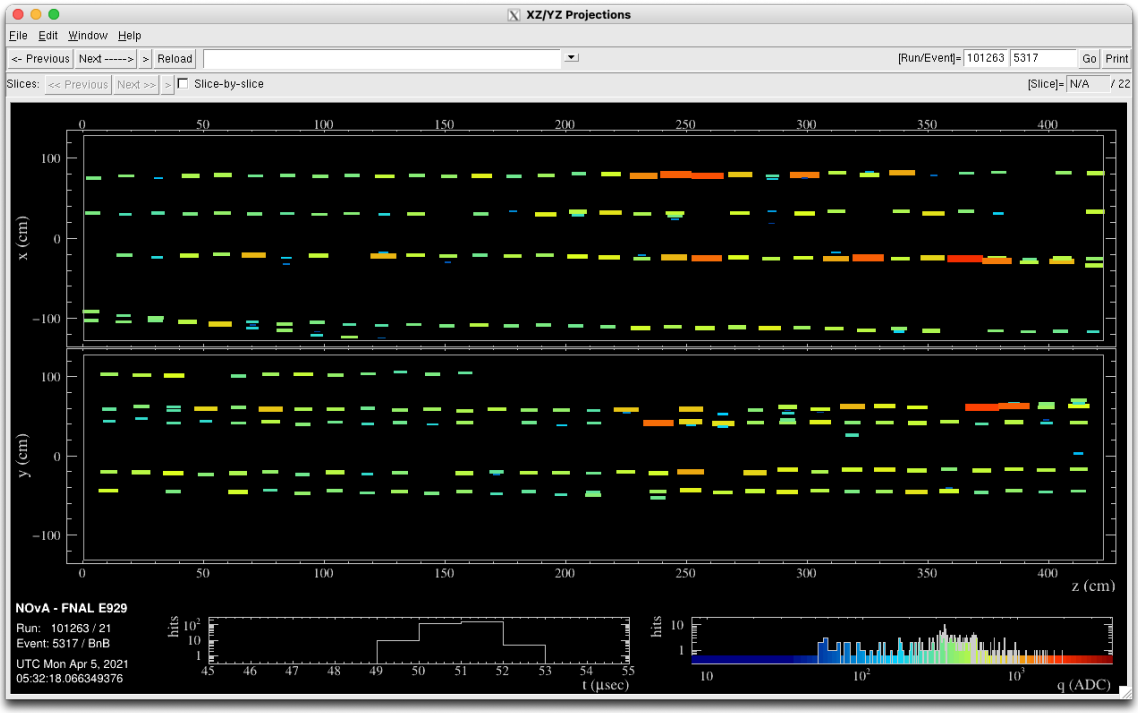

Figure C.1: A proton in the event display.

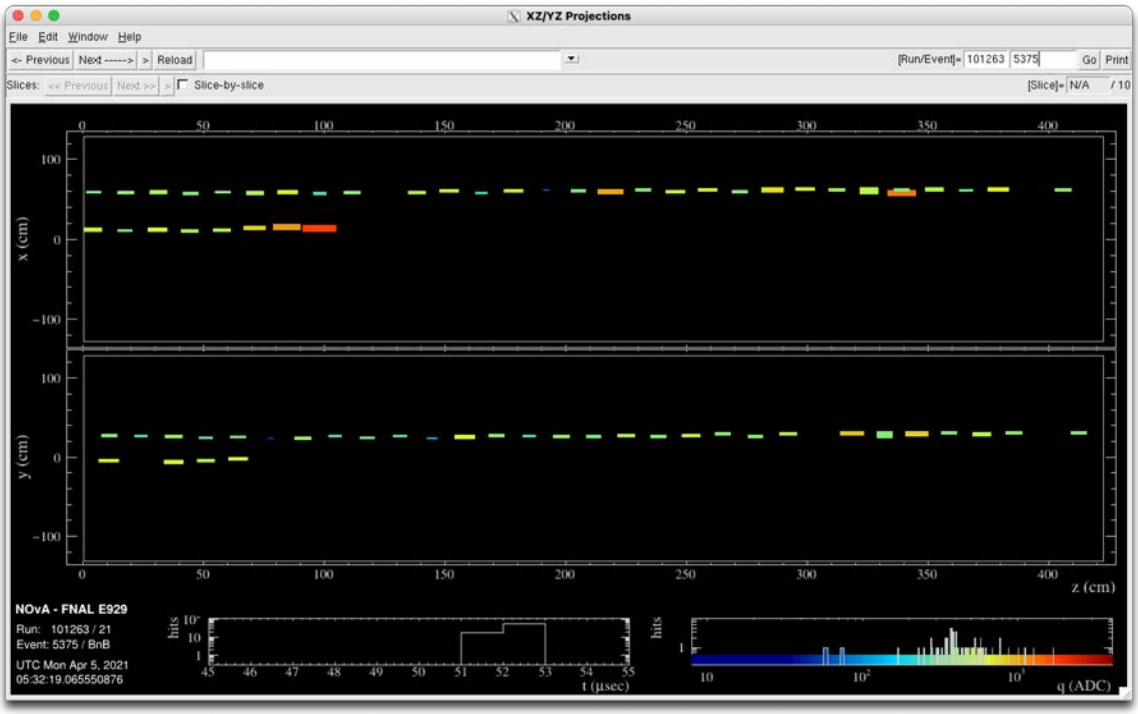

Figure C.2: A proton in the event display.

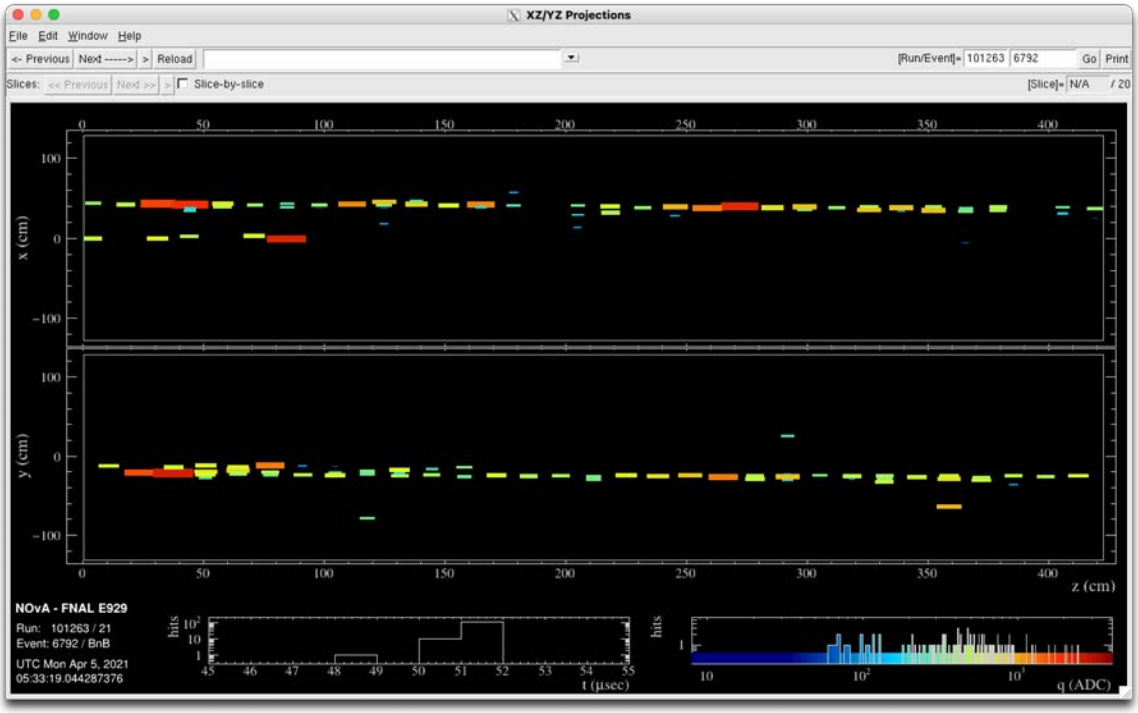

Figure C.3: A proton in the event display.

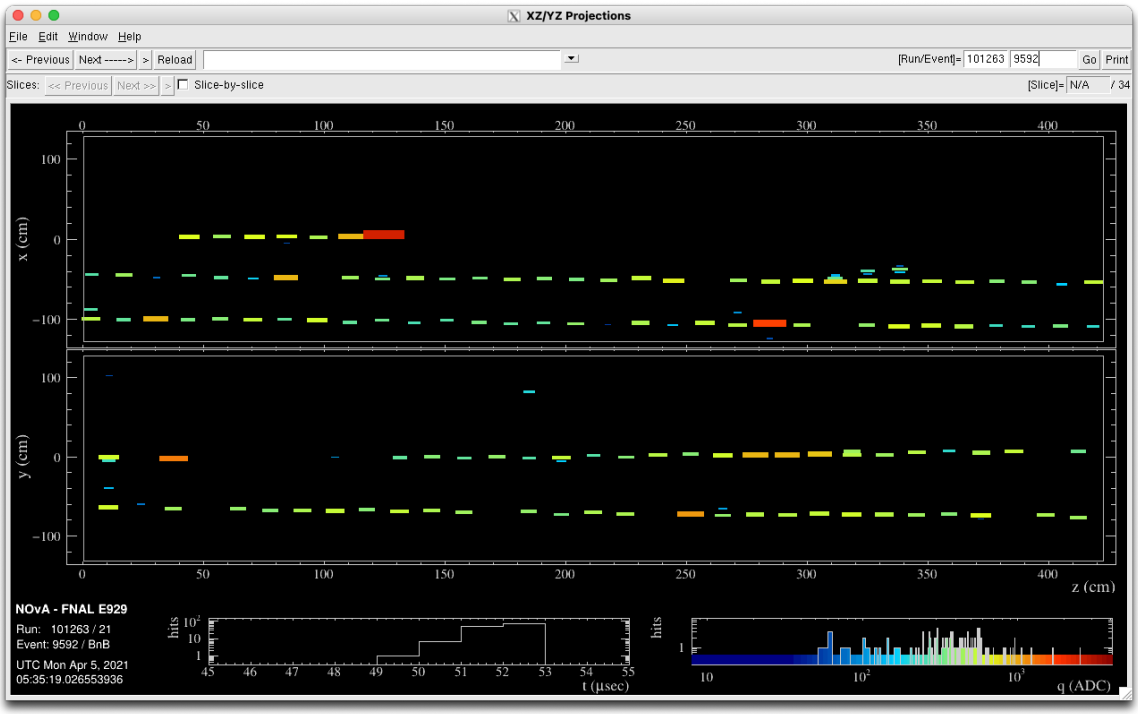

Figure C.4: A proton in the event display.

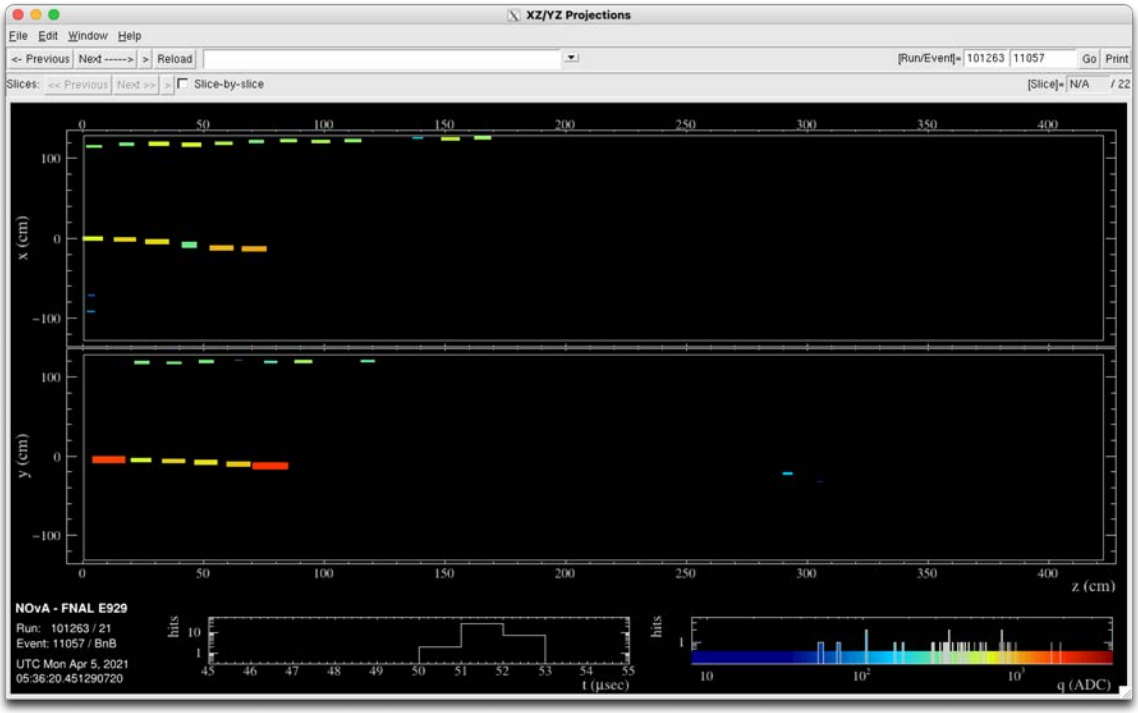

Figure C.5: A proton in the event display.

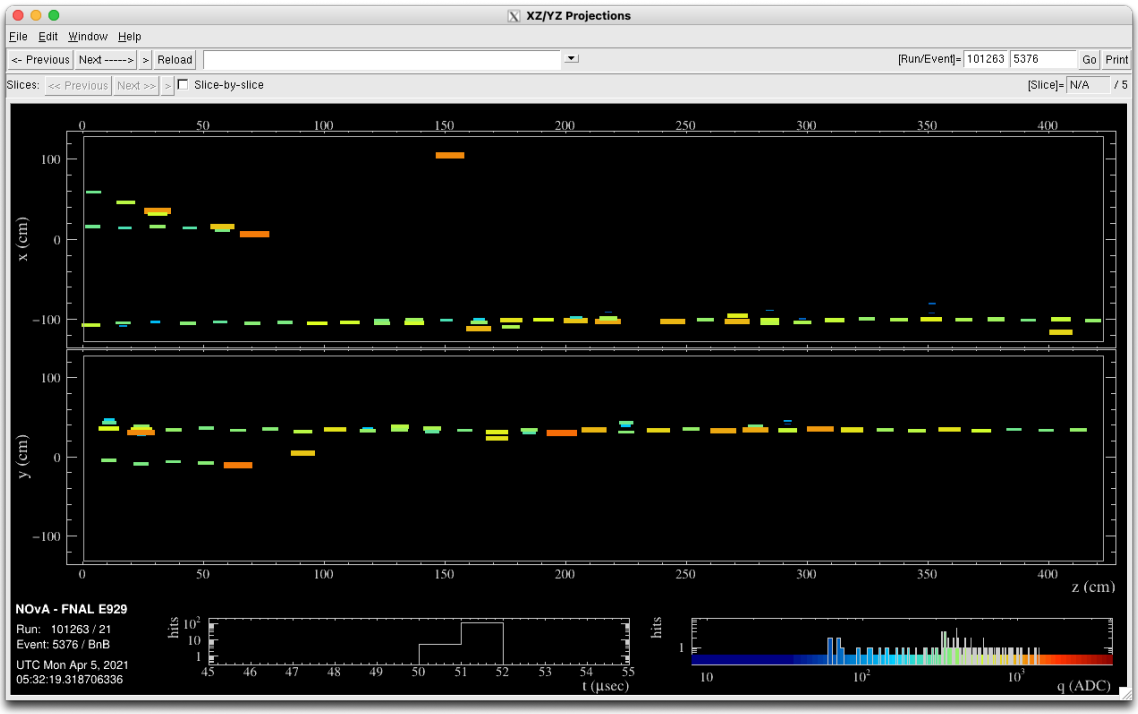

Figure C.6: A pion or muon in the event display.

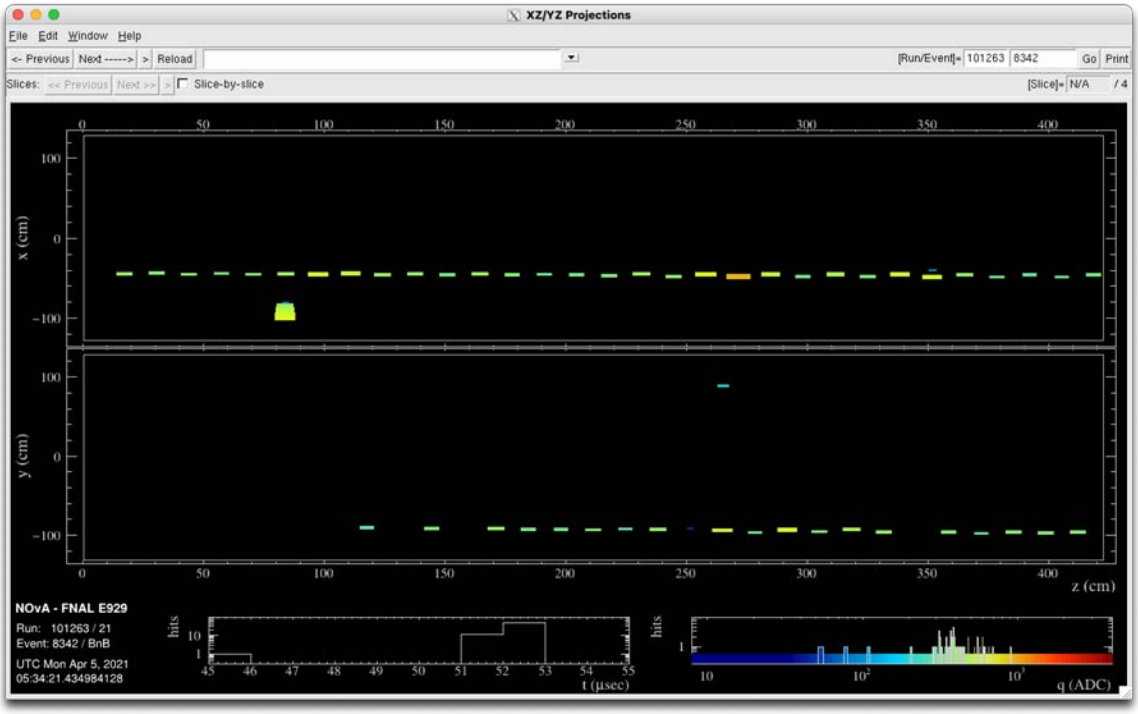

Figure C.7: A pion or muon in the event display.

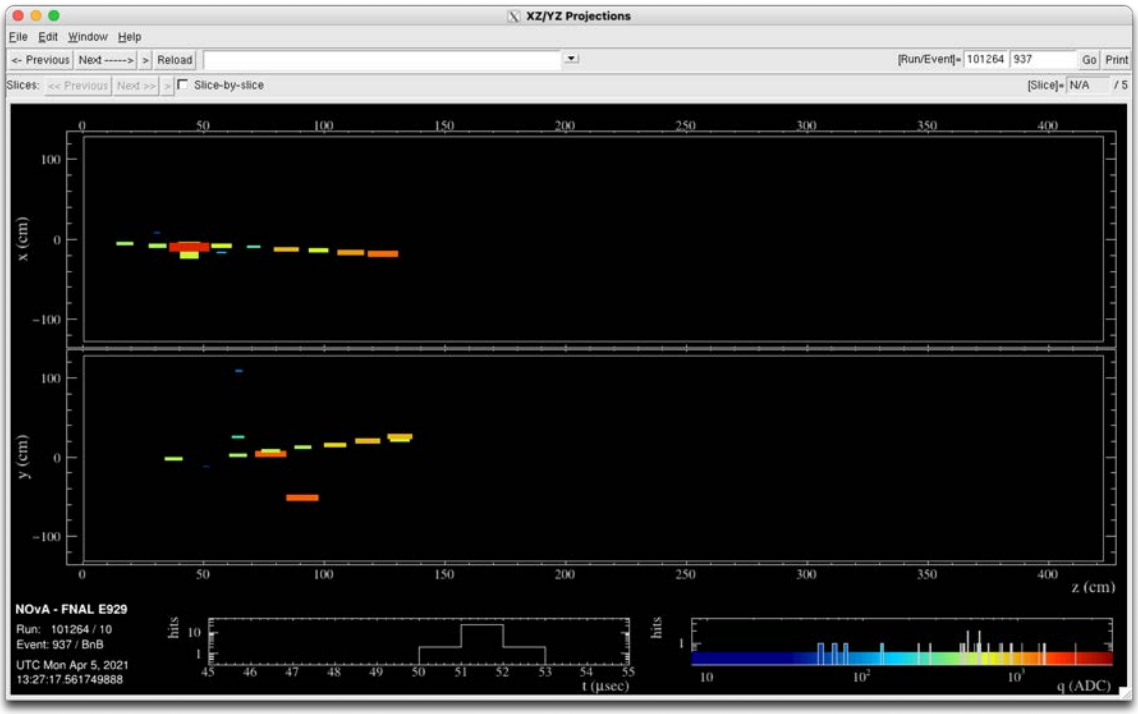

Figure C.8: A pion or muon in the event display.

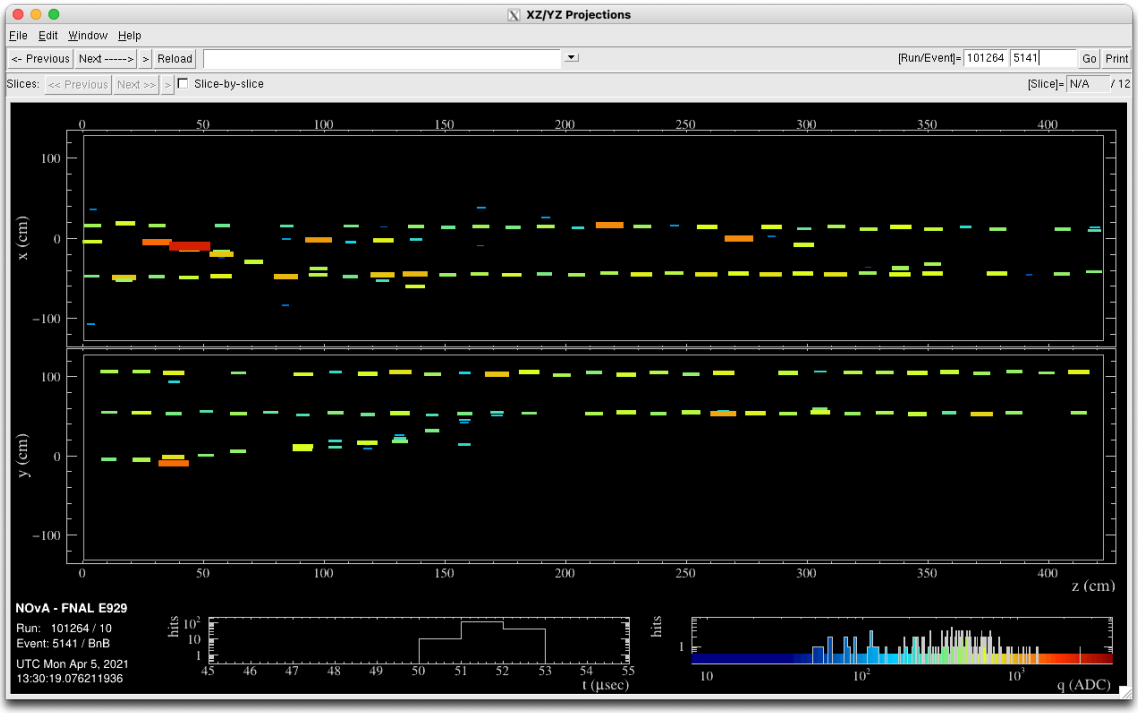

Figure C.9: A pion or muon in the event display.

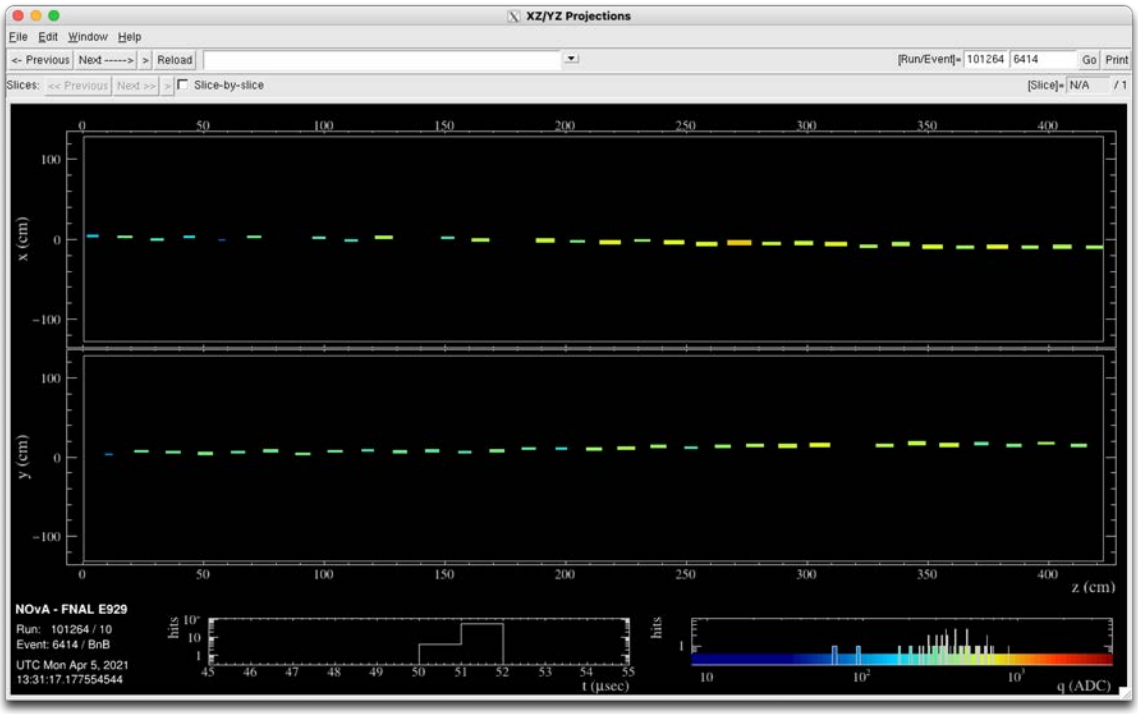

Figure C.10: A pion or muon in the event display.

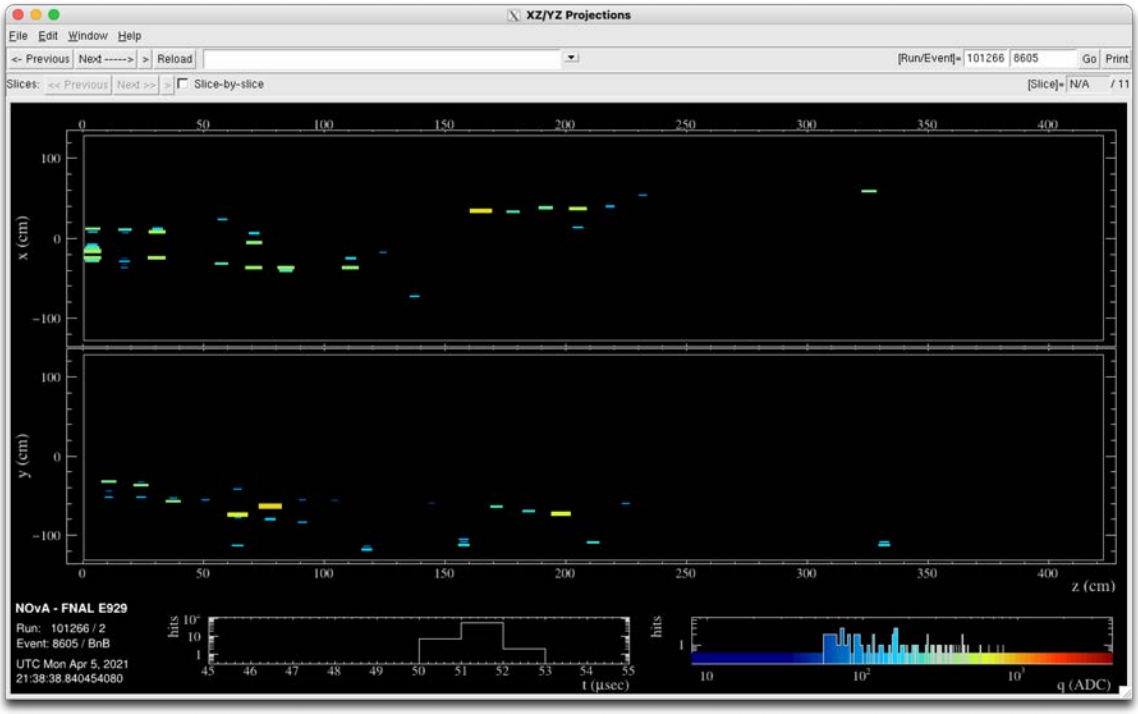

Figure C.11: An electron in the event display.

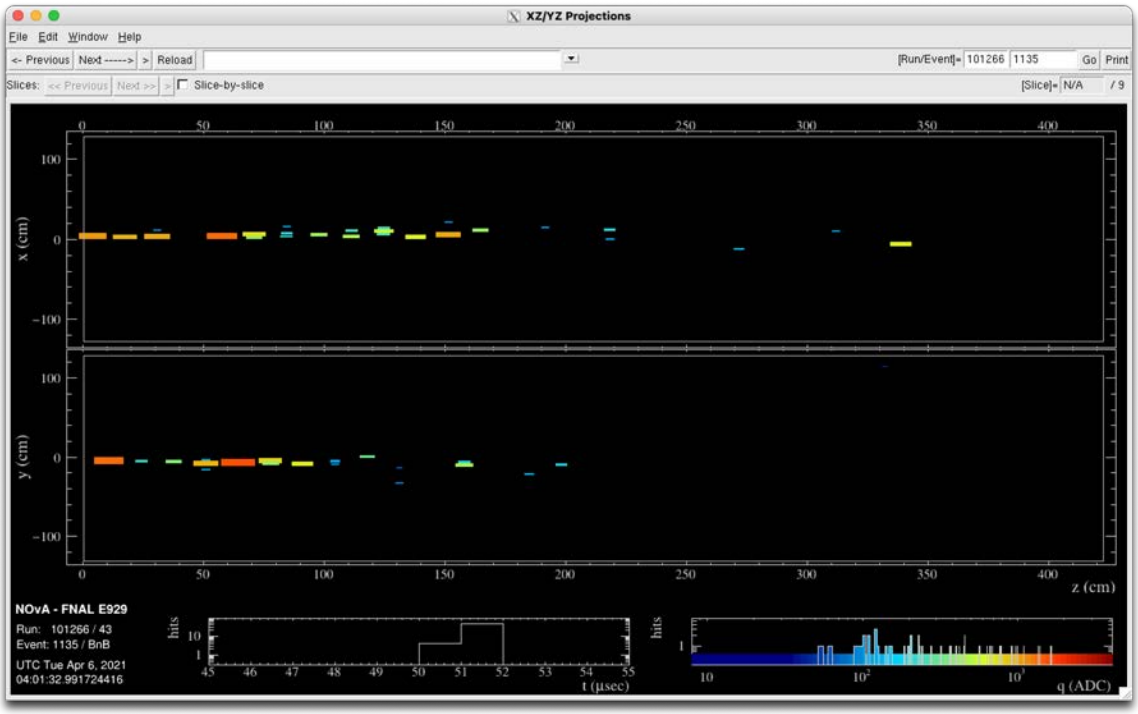

Figure C.12: An electron in the event display.

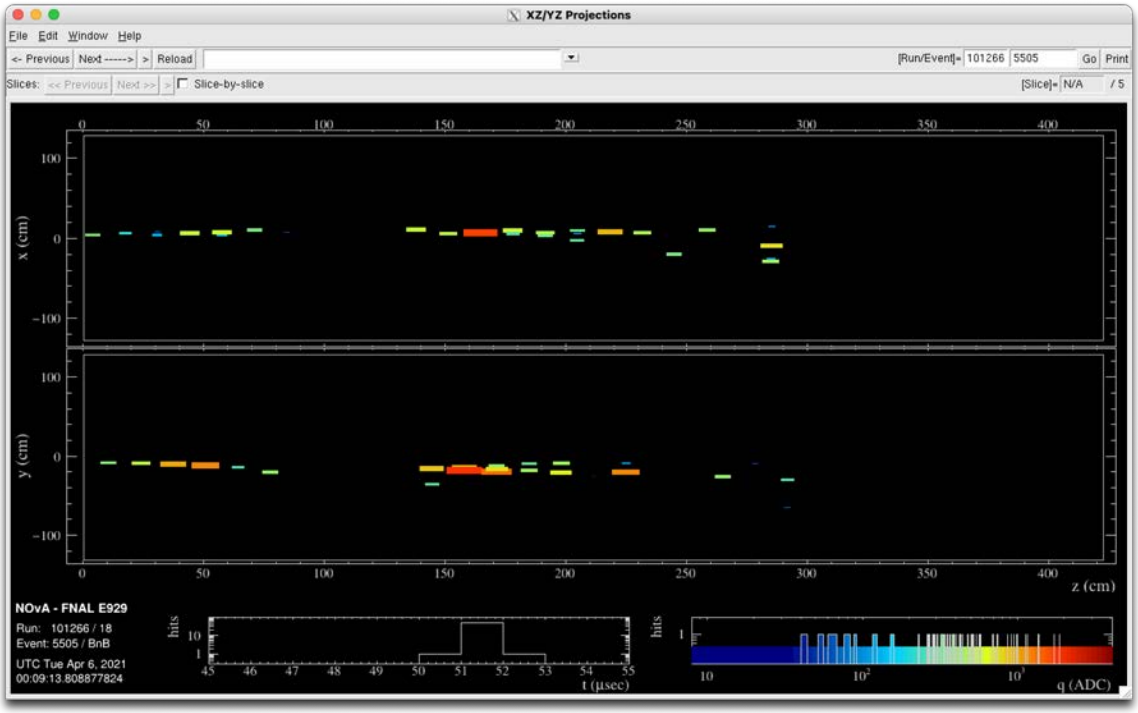

Figure C.13: An electron in the event display.

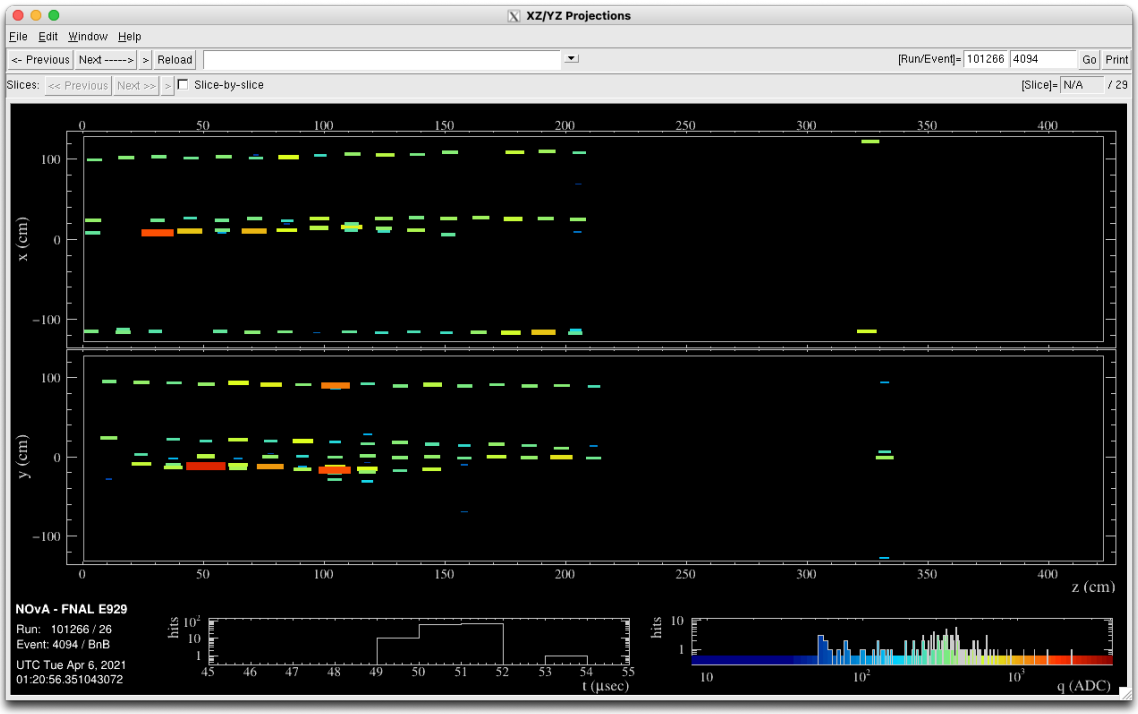

Figure C.14: An electron in the event display.

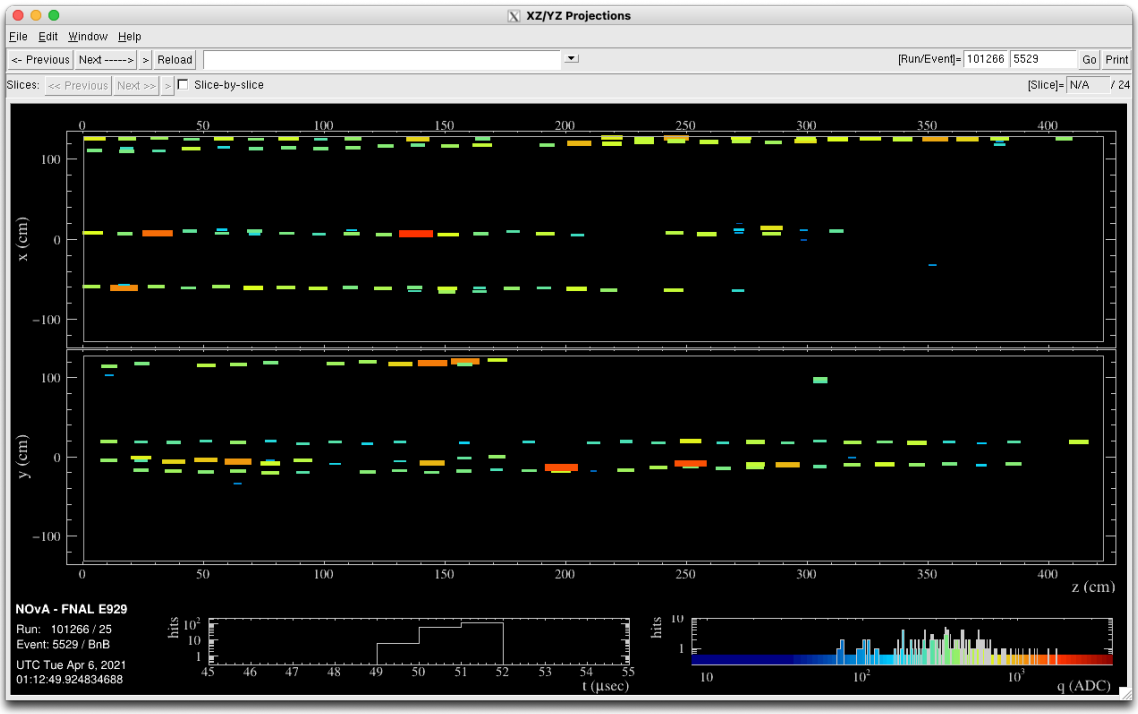

Figure C.15: An electron in the event display.

Bibliography

[1] Y. Farzan and M. Tórtola, Front. Phys. **6**, 10 (2018).

[2] P. Adamson et al. (NOνA Collaboration), Phys. Rev. D **93**, 051104(R) (2016).

[3] M. Rominsky et al. (Fermi Research Alliance), Fermilab Test Beam Facility Annual Report: FY19, FERMILAB-TM-2702, 2019.

[4] T. Lackey (private communication), 2020.

[5] G. Pulliam, PhD Dissertation, Syracuse University, 2019.

[6] B. Fox, J. Huang, K. Lang, D. Phan, M. Proga, and B. Tapia, The University of Texas at Austin, "Cherenkov Counter for NOνA's Test Beam," 2019.

[7] T. Lackey and M. Messier, "New Magnetic Field (Beff) and momentum reconstruction" (NOνA docdb-47494), 2020.

[8] M. Wallback (private communication), 2021.

[9] S. Block (private communication), 2021.

[10] M. Wallback (private communication), 2021.

[11] D. Phan (private communication), 2020.

[12] Y. Torun, "Acceptance and scattering in TOF walls" (NOνA docdb-48453), 2020.

[13] A. Sousa, "Test Beam TOF Redeployment Discussion Slides" (NOνA docdb-48480), 2020.

[14] T. Lackey (private communication), 2021.